Membrane Binding Controls the ATPase Cycle and Localization of MinD in *Bacillus subtilis*

Helge Feddersen[1], Charlotte Dyckmanns[1] and Marc Bramkamp[1,*]

[1] *Institute for General Microbiology, Christian-Albrechts-University Kiel, Am Botanischen Garten* 1-9, 24118 Kiel, Germany

Running title: MinD dynamics in *B. subtilis*

*To whom correspondence should be addressed: Marc Bramkamp, Christian-Albrechts-University Kiel, Institute for General Microbiology, Am Botanischen Garten 1-9, 24118 Kiel, Germany, Email: bramkamp@ifam.uni-kiel.de; Phone: +49 (0)431-880-4341; Telefax: +49(0)431-880-2198
Bluesky: @bramkamplab.bsky.social

Abstract

Bacteria precisely regulate the place and timing of their cell division. One of the best-understood systems for division site selection is the Min system in *Escherichia coli*. In *E. coli*, the Min system displays remarkable pole-to-pole oscillation, creating a time-averaged minimum at the cell's geometric center, which marks the future division site. Interestingly, the Gram-positive model species *Bacillus subtilis* also encodes homologous proteins: the cell division inhibitor MinC and the Walker-ATPase MinD. However, *B. subtilis* lacks the activating protein MinE, which is essential for Min dynamics in *E. coli*. We have shown before that the *B. subtilis* Min system is highly dynamic and quickly relocalizes to active sites of division. This raised questions about how Min protein dynamics are regulated on a molecular level in *B. subtilis*. Here, we show with a combination of *in vitro* experiments and *in vivo* single-molecule imaging that the ATPase activity of *B. subtilis* MinD is activated solely by membrane binding. Additionally, both monomeric and dimeric MinD bind to the membrane, and binding of ATP to MinD is a prerequisite for fast membrane detachment. Single-molecule localization microscopy data confirm membrane binding of monomeric MinD variants. However, only wild type MinD enriches at cell poles and sites of ongoing division, likely due to interaction with MinJ. Monomeric MinD variants and locked dimers remain distributed along the membrane and lack the characteristic pattern formation. Single-molecule tracking data further support that MinD has a freely diffusive population, which is increased in the monomeric variants and a membrane binding defective mutant. Thus, MinD dynamics in *B. subtilis* do not require any unknown protein component and can be fully explained by MinD's binding and unbinding kinetics with the membrane. The spatial organization of MinD relies on the short-lived temporal residence of MinD dimers at the membrane.

Keywords

B. subtilis, Min system, cell division, ATPase, membrane binding, protein patterns, reaction diffusion, self-organization, SMLM, SMT

Introduction

Accurate selection of the division site is essential in bacteria for maintaining cell size, ensuring proper chromosome segregation, and preventing the formation of anucleate minicells. Cell division is governed by a complex protein machine known as the divisome (3-5). The spatiotemporal organization of this protein complex is directed by the dynamic arrangement of a bacterial tubulin homolog, FtsZ (6, 7). FtsZ forms treadmilling protofilaments that condense into a ring-like structure at the division site (8-10), recruiting several cell wall synthesis proteins, such as division-specific transglycosylases and transpeptidases (11, 12). Together, these proteins synthesize the bacterial peptidoglycan cell wall. To ensure that FtsZ polymerizes only at the correct location, many bacterial species employ the Min system, a conserved pathway that prevents aberrant polar septation events.

The Min system was identified through the formation of small, round, anucleate cells that divide close to the cell poles (27). The gene locus responsible for the "*min*iature" cell phenotype in *E. coli* was termed *minB* (28, 29), later shown to encode the three structural genes *minC*, *minD* and *minE* (30). MinC is the actual inhibitor of FtsZ-polymer formation (31, 32). The MinC protein contains an N- and C-terminal domain (33), both of which contribute to FtsZ inhibition. The C-terminal domain binds to the C-terminal tail of FtsZ, whereas the N-terminal domain, which also mediates MinC dimerization, binds at the interface of two FtsZ subunits (34-36). MinC-mediated inhibition of FtsZ has also been demonstrated in *B. subtilis* (37-39), suggesting a conserved mechanism across species.

The spatial localization of MinC is regulated by MinD, a Walker-type ATPase that belongs to the ParA/MinD family of proteins (37, 40, 41). These partitioning ATPases are involved in positioning cargo within bacterial cells (42, 43). While the molecular details of partitioning

69 differ among ParA-like proteins, a common feature is their use of binding to a large
70 intracellular surface as a spatial template (42, 43). ParA proteins typically bind non-
71 specifically to DNA, covering the nucleoid and exploiting it as a track for cargo positioning
72 (44). In contrast, MinD proteins bind to the membrane via an amphipathic helix (45, 46). In *E.*
73 *coli*, membrane binding of MinD strictly depends on ATP binding and subsequent
74 dimerization (40). Dimerized MinD recruits MinC and thereby activates MinC to inhibit FtsZ
75 oligomerization. In *E. coli*, MinE further regulates MinD localization by binding to the
76 membrane and interacting with MinD, stimulating ATP hydrolysis and triggering MinD
77 release from the membrane. Slow nucleotide exchange in cytosolic MinD leads to an
78 oscillatory cycle of membrane attachment and detachment, resulting in pole-to-pole
79 oscillation of MinCD (48-50). This oscillatory behavior generates a temporal minimum of
80 MinC at midcell, such that Z-ring assembly is restricted exclusively to this position. The
81 oscillation can be reconstituted *in vitro* on planar membranes, demonstrating the robustness
82 of this self-organizing system and a prime example of pattern formation. (51).

83 The Gram-positive model bacterium *B. subtilis* likewise encodes the *minC* and *minD* genes
84 (52, 53), and loss of either results in the characteristic minicell phenotype. Thus, a role for
85 the Min system analogous to that in *E. coli* has been proposed (37, 54). However, *B. subtilis*
86 lacks a MinE homolog, and the Min proteins do not oscillate from pole to pole (37, 54).
87 Instead, static imaging shows that MinD accumulates at the cell poles and at active division
88 sites. Initial genetic and cell biological studies demonstrated that the polar scaffold protein
89 DivIVA is essential for polar MinD localization (37). The interaction between DivIVA and
90 MinD is mediated by the integral membrane protein MinJ (55, 56). MinJ is also part of the
91 divisome and interacts with multiple division proteins (56). Loss of MinJ causes defects in
92 divisome disassembly, as proteins such as FtsL and PBP2b remain associated with the

93 nascent cell pole after division in Δ*minJ* cells (57). This function is supported by recent
94 findings that MinD promotes FtsZ polymer disassembly at the cell poles, and that deletion of
95 *minD* inhibits polar peptidoglycan remodeling (58).

96 We have recently shown that all components of the *B. subtilis* Min system, including DivIVA
97 and MinJ, dynamically localize within the bacterial cell (57, 59-61). Interestingly, even the
98 scaffold protein DivIVA, although highly conserved in many Gram-positive phyla, is not
99 statically anchored at the poles but instead redistributes along the membrane from poles to
100 septa (59-61). In contrast, DivIVA homologs in actinobacteria show greatly reduced mobility,
101 consistent with their role in apical growth (60).

102 Despite these advances, the mechanism by which MinD activity and localization are
103 regulated in the absence of MinE has remained unclear, raising the possibility of additional,
104 unidentified regulatory factors or alternative modes of ATPase control. In this study, we
105 address these long-standing questions by combining *in vitro* biochemical analyses with
106 single-molecule imaging *in vivo*. We define the ATPase and membrane-binding properties of
107 *B. subtilis* MinD and examine how its dynamics are shaped by interactions with MinJ and
108 MinC. Our findings reveal an unexpected mechanism of MinD regulation that operates
109 independently of MinE-like factors, providing a revised understanding of how the non-
110 oscillatory *B. subtilis* Min system robustly controls cytokinesis and prevents aberrant
111 septation events.

Results

Purification and gel filtration of His-MinD

Since localization and function of MinD appear to be strongly tied to its ATPase activity, the first logical step in describing and understanding details of the ATPase cycle was identification of the relevant biochemical characteristics, to eventually be able to correlate these properties to *in vivo* observations. To this end, *B. subtilis minD* was heterologously expressed in *E. coli*, yielding an N-terminally His-tagged fusion protein (Fig. S 1), as C-terminal MinD fusions have been shown to interfere with membrane binding (62). Since MinD is known for being membrane-associated, a well-established *E. coli* MinD purification protocol was adapted (63), where buffers were supplied with excess Mg^{2+}-ADP to potentially reduce MinD self- and membrane interaction. Based on the respective western blot and gel filtration chromatogram (Fig. S 1 and Fig. S 2), His-MinD is not able to dimerise when purified in presence of excess Mg^{2+}-ADP, as evidenced by a main peak at the expected sizes of the monomeric form (~31 kDa, 16.11 ml) and the absence of a peak at the expected size of the dimeric form (~62 kDa, 14.65 ml, Fig. S 2). However, Western blotting of Ni-NTA and size-exclusion chromatography (SEC) fractions indicates the presence of multiple His-tagged degradation products alongside full-length His-MinD (Fig. S 1). Because these fragments retain the His-tag, they co-purify during Ni-NTA and can co-elute or form non-covalent assemblies with full-length MinD, increasing the heterogeneity of the sample and likely producing the minor shoulder observed at an apparent molecular weight of ~44 kDa (15.4 ml, Fig. S 2). Unfortunately, the Mg^{2+}-ADP excess in the purification buffers did not seem to stop His-MinD membrane interaction, as a significant fraction of the recombinant protein

135 were later detected to be lost in the cell pellet. However, sufficiently high His-MinD
136 concentrations could be obtained to proceed with biochemical analysis.

137 ***B. subtilis* MinD displays full ATPase activity when incubated with ATP and liposomes.**

138 Being able to purify His-MinD allowed us to investigate the biochemical conditions affecting
139 the MinD ATPase cycle next. For this purpose, we choose to use the commercially available
140 enzyme coupled EnzChek™ phosphate assay kit (Thermo Fisher Scientific) to measure
141 ATPase activity. The activity was determined by measuring the P_i production rate (in µM
142 min^{-1}) as a function of His-MinD concentration. We first tested His-MinD ATPase activity at
143 protein concentrations between 0.5 µM and 16 µM. Under these conditions, only baseline
144 ATPase activity below the detection limit was observed (consistent with Fig. 1 D, 0 mg ml^{-1}
145 liposomes condition). Since MinD interacts with the membrane and it was expected that the
146 ATPase cycle is involved in controlling this interaction, we next measured ATPase activity in
147 the presence of liposomes extruded from *E. coli* total lipids (Avanti). Remarkably, this led to
148 a robust increase in ATPase activity of His-MinD, appearing to be linearly dependent on
149 protein concentration (Fig. 1 A & B). To be able to compare the activity level to the published
150 *E. coli* MinD *in vitro* ATPase data (64-66), the specific activity is shown as a specific activity in
151 nmol mg^{-1} min^{-1} (Fig. 1 B). Interestingly, activity levels of recombinant *B. subtilis* MinD were
152 found to be on par with fully active *E. coli* MinD in conjunction with MinE and phospholipids
153 (64). Moreover, the ATPase activity did not show cooperative behavior compared to *E. coli*
154 MinD at lower concentrations (64). We further measured that ATP hydrolysis can be titrated
155 with both ATP and liposomes and is described by Michaelis-Menten kinetics (Fig. 1 C & D).
156 Again, the hereby-obtained V_{max} values (19.50 nmol mg^{-1} min^{-1} and 22.05 nmol mg^{-1} min^{-1},
157 respectively) indicate similar ATPase activity levels between MinD from *E. coli* and *B. subtilis*.

158 **MinC and the PDZ domain of MinJ have different effects on MinD ATPase activity**

159 Even though ATPase activity levels were similar, proteins that directly interact with MinD
160 could potentially modulate this activity *in vivo* as seen for MinD:MinE in *E. coli* (64-66). To
161 get the complete picture of MinD activity, investigating the potential effects of both known
162 *B. subtilis* MinD interactors MinC and MinJ was therefore necessary. For this purpose, both
163 proteins were subjected to purification attempts. While purification of the cytosolic His-
164 MinC could be successfully established using affinity chromatography followed by SEC (Fig. S
165 3), the intermembrane protein His-MinJ proved more challenging. Since several different
166 purification attempts of the full-length protein yielded no stable product, a truncated form
167 containing only the soluble C-terminal PDZ domain of MinJ fused to an N-terminal His-tag
168 (His-PDZ) via a flexible linker was expressed instead (Fig. S 4). PDZ domains are often found
169 in membrane-associated proteins and known to selectively interact with the C-terminus of
170 partner peptides or proteins to sequester them to highly specific sites of the cell, both in
171 pro- and eukaryotes (67). Although His-PDZ could be isolated via Ni-NTA affinity
172 chromatography, it was unstable during SEC and consistently lost from the column,
173 precluding further purification by this method. Hence, further experiments were performed
174 using His-PDZ directly after affinity chromatography.

175 To test the effect of His-MinC and His-PDZ on His-MinD ATPase activity, the previously
176 established enzymatic assays were repeated in the presence of either His-MinC or His-PDZ
177 (Fig. S 5). Addition of His-MinC resulted in a very small but statistically significant decrease in
178 MinD ATPase activity (~5%). Given the small sample size this effect should be interpreted
179 cautiously. However, it could be caused by the experimental set-up, since the high amounts
180 of MinC (6 µM) that have been used might sequester a small fraction of MinD away from

181 membrane surfaces that are required for efficient ATP hydrolysis, due to direct interaction of
182 MinC and MinD.

183 In contrast, addition of His-PDZ led to a slight but reproducible increase in MinD ATPase
184 activity, which prompted us to repeat the experiment at different His-PDZ concentrations
185 (Fig. S 5). All His-PDZ concentrations significantly increased His-MinD ATPase activity
186 compared to the control (1 µM His-PDZ = 25% ± 6.8%, 3 µM His-PDZ = 37 ± 12.5 %; 5 µM His-
187 PDZ = 22% ± 2.8 %). We speculate that the PDZ domain may promote MinD:MinD
188 encounters, facilitating dimerization rather than directly enhancing catalytic turnover.
189 Because only the soluble PDZ domain could be purified, it remains unclear how full-length,
190 membrane-anchored MinJ would influence MinD activity in vivo. The magnitude of the
191 effect might differ when the PDZ domain is present in its native membrane-associated
192 context.

193 **MinD ATPase activity is triggered by membrane binding**

194 To determine whether interaction with the membrane is sufficient to stimulate MinD ATPase
195 activity, a MinD mutant that is defective in membrane binding was required. MinD interacts
196 with the membrane through an amphipathic α-helix located at the N-terminus, thus being
197 the membrane targeting sequence (MTS) (Fig. 2 A). Exchanging the hydrophobic isoleucine
198 residue in the apolar core of the MTS with a charged glutamate (I260E) has been shown to
199 abolish membrane binding of MinD by perturbing the amphipathic properties, demonstrated
200 through fluorescence microscopy (68). Accordingly, a His-MinD-I260E variant was
201 constructed and purified via the established purification protocol. The yield of the
202 purification was extensively higher compared to the wild type protein (Fig. S 6), hinting
203 towards a successful abolishment of membrane interaction.

204 We next repeated ATPase activity assays with the purified, recombinant I260E mutant, and
205 remarkably, activity remained below the detection limit of the assay, while a positive control
206 of His-MinD wild type protein displayed regular activity (Fig. S 7). In summary, these data
207 collectively suggest that membrane binding is necessary and the key trigger for ATP
208 hydrolysis of *B. subtilis* MinD, without the apparent need for another stimulus.

209 Next, we wanted to compare *in vivo* and *in vitro* data. Therefore, a *B. subtilis* strain for
210 microscopy was constructed, where the native copy of MinD was replaced by a HaloTag-
211 MinD fusion protein (Fig. 2 B, HaloTag will henceforth be referred to as Halo). We then
212 introduced the I260E mutation, resulting in a strain producing Halo-MinD-I260E as the only
213 copy. Microscopic analysis of a Halo-MinD-I260E with TMR dye confirmed drastically
214 reduced membrane binding through its almost exclusive cytosolic localization (Fig. 2 B).
215 Furthermore, cell length and the number of minicells increased drastically, comparable to a
216 *minD* knockout (Tab. S 1).

217 **Construction of catalytic MinD mutants**

218 To determine the role of ATP-mediated dimerization in membrane binding, we explored
219 further mutations that affect the ATP binding region and thus the dimerization process. Due
220 to the conserved nature of Walker-type MinD/ParA-like ATPases, residues involved in
221 catalytic activity have been well characterized (69-71). We therefore constructed expression
222 plasmids encoding three different MinD variants (illustrated in Fig. 2 A): This first mutation,
223 MinD-G12V, produces a steric clash within the active site, so that ATP can still be bound, but
224 dimers cannot form (69, 70). The second mutation, K16A, completely disrupts ATP binding
225 and hence results in monomeric protein (69). The third variant encodes the mutation D40A,
226 which should interfere with ATP hydrolysis (70, 71). Therefore, it was expected that MinD-

227 D40A forms a trapped nucleotide sandwich dimer similar to Soj or *E. coli* MinD (70, 71). All
228 MinD variants were successfully expressed and purified and resulted in similar protein yields
229 when compared to the wild type protein (Fig. S 1, Fig. S 8, Fig. S 9 and Fig. S 10). When
230 evaluating the gel filtration chromatograms, His-MinD-G12V elute in a single peak, which can
231 be interpreted as a monomer when compared to the wild type His-MinD elution peak (Fig. S
232 2). His-MinD-D40A on the other hand also eluted in a single peak, albeit being wider and
233 eluting earlier, indicating a mainly dimeric conformation. It eluted between the expected
234 dimer and monomer positions during SEC as a wide peak (Fig. S 2). As His-MinD-D40A cannot
235 hydrolyze ATP, it should be dimeric and likely also form small oligomers or transient
236 multimers. A mixture of monomer/dimer/oligomer likely produced the broad, left-shifted
237 peak whose center is between monomer and dimer. Only His-MinD-K16A reproducibly
238 formed a rather unexpected shoulder in its main elution peak, which could hint towards
239 further interaction with the gel filtration matrix or other potential self-interactions. All of the
240 recombinant His-MinD mutants displayed negligible ATPase activity when tested using the
241 EnzChek phosphate assay kit (Fig. S 7 C). This was expected, as all of these MinD variants
242 (G12V, K16A and D40A) were mutated in residues which significantly alter the ATP binding
243 site. In all cases, activity levels remained consistently near the detection limit, precluding
244 reliable quantitative interpretation.

245 To investigate *in vivo* effects of these variants, the same mutations were introduced into the
246 strain expressing Halo-MinD in *B. subtilis*, respectively, and subsequently imaged via wide-
247 field microscopy (Fig. 2 B). All strains producing MinD mutants displayed an increased cell
248 length and minicell production comparable to Δ*minD* (Tab. S 1), as it was expected in cells
249 containing dysfunctional Min proteins. Surprisingly, both monomeric MinD variants (G12V
250 and K16A) were still observed to be membrane associated, however resulting in the

251 apparent loss of the polar-septal MinD localization (Fig. 2 B). Finally, the locked dimer D40A
252 mutant appeared to be mainly membrane associated, thereby forming large foci indicating
253 accumulation of MinD, but much less dispersed when compared to G12V or K16A (Fig. 2 B).
254 In summary, the time-resolved MinD gradient appears to be lost in all MinD mutants,
255 including D40A. This suggests that the ATPase cycle and thus quick cycling of MinD is indeed
256 necessary for formation of the observed dynamic gradient, as it has been previously
257 suggested (61).

258 **Monomeric MinD binds the membrane with high efficiency.**

259 Membrane binding appeared to be a key factor of the ATPase cycle and since the
260 microscopy-data indicated binding of MinD monomers to the membrane, we next aimed to
261 determine biochemically, if the respective MinD variants are capable of binding to
262 membrane and if so, to characterize their respective binding kinetics. To this end, we
263 employed Bio-layer interferometry (BLI), a technique capable of quantifying binding strength
264 and protein interaction, as well as identifying reaction kinetics. Liposomes were immobilized
265 on a biosensor to create a membrane-like surface for subsequent MinD binding assays. After
266 successful saturation of the sensor with liposomes, MinD-liposome association and
267 dissociation was measured, a scheme of the experimental set-up is depicted in Fig. 3 A. As a
268 negative control for unspecific binding, MinD-sensor interaction was tested on empty SA
269 sensors. Furthermore, unspecific binding to liposome-saturated sensors was tested using
270 bovine serum albumin (BSA). Both resulted in negligible, diffuse signal (data not shown).

271 Kinetics of His-MinD binding was tested first, using different protein concentrations between
272 1 µM and 16 µM in presence of ATP. Binding to the sensor-bound liposomes scaled with
273 increasing protein concentration, resulting in an equilibrium dissociation constant K_D = 7.17

274 µM and an association rate constant k_{on} = 3.03 x 10^3 M^{-1} s^{-1} as a reference point for the wild
275 type protein (Fig. 3 B, Tab. 1**Error! Reference source not found.**). Unsurprisingly, His-MinD-
276 I260E showed a more than 10-fold reduced affinity to the membrane with a K_D = 74.36 µM
277 (Tab. 1**Error! Reference source not found.**), which is also apparent in the binding graph (Fig.
278 3 B). The strong increase in K_D is based on the over 16-fold lowered association k_{on} = 0.18 x
279 10^3 M^{-1} s^{-1}, while the dissociation k_{off} = 13.45 x 10^{-3} s^{-1} was also slightly lower when compared
280 to wild type MinD. Next, both monomeric mutants G12V and K16A were probed, and to our
281 surprise, capable of membrane interaction (Fig. 3 C & D, **Error! Reference source not**
282 **found.**). This is in stark contrast to *E. coli* MinD, where dimerization needs to precede
283 membrane binding to achieve sufficient affinity (45, 46, 65, 71, 72). Similar to I260E, the
284 G12V mutant displayed an around 10-fold reduced membrane affinity equilibrium with K_D =
285 75.38 µM (Tab. 1**Error! Reference source not found.**). However, G12V only exhibited a ~5
286 fold reduced binding affinity with k_{on} = 0.63 x 10^3 M^{-1} s^{-1} when compared to the wild type
287 MinD, while the k_{off} = 47.8 x 10^{-3} s^{-1} represents the fastest dissociation rate constant
288 between all MinD variants and more than 2-fold increase compared to wild type MinD (Tab.
289 1**Error! Reference source not found.**). This indicates a higher turnover and thus a quicker
290 release of the protein from the membrane. Markedly different from this, K16A displayed a
291 K_D of 1.36 µM, but not much lower binding rates (k_{on} = 2.03 x 10^3 M^{-1} s^{-1}, Tab. 1**Error!**
292 **Reference source not found.** & Fig. 3 C). Instead, the low K_D can be mostly attributed to the
293 reduced dissociation (k_{off} = 2.77 x 10^{-3} s^{-1}), implying a much longer retention of His-MinD-
294 K16A at the membrane (Fig. 3 D). Since G12V can bind ATP while K16A cannot, these findings
295 reveal that presence of ATP in the binding pocket affects association and dissociation of
296 MinD.

297 Last, the His-MinD-D40A mutant protein was probed, resulting in an almost 10-fold reduced
298 dissociation equilibrium K_D = 0.74 µM (Tab. 1**Error! Reference source not found.**, Fig. 3 E).
299 Here, the strongly reduced membrane dissociation (k_{off} = 1.76 x 10^{-3} s^{-1}) causes the drastic
300 change in K_D, which we expected for the trapped dimer, as it could position the two
301 amphipathic helices into a more optimal orientation of the apolar residues towards the
302 membrane, resulting in stronger binding and no capability of hydrolyzing ATP and thus
303 relieving the dimer (68, 70, 71).

304 In summary, these BLI data demonstrate that *B. subtilis* MinD is capable of binding
305 membrane in both monomeric and dimeric form, while the presence of ATP in the binding
306 pocket appears to affect both membrane binding and dissociation.

307 **MinC and the PDZ-domain of MinJ have no significant impact on MinD membrane kinetics.**

308 *In vivo*, the integral membrane protein MinJ recruits MinD to poles and septum, which in
309 turn recruits MinC to form a functional complex that inhibits FtsZ-ring assembly. However,
310 the mechanistic details of how MinJ influences membrane association of MinD remain
311 unclear. Does MinJ actively recruit MinD from the cytoplasm, or does it primarily sequester
312 MinD already bound to the membrane? Furthermore, does MinJ promote MinD dimerization
313 or oligomerization, potentially enhancing ATPase activity and triggering membrane
314 dissociation? Similarly, MinC binding to MinD may influence the stability or turnover of MinD
315 at the membrane, yet its impact on association/dissociation kinetics is unknown. To address
316 these questions directly, we employed BLI to test the effect of His-MinC and His-PDZ on His-
317 MinD membrane kinetics.

318 After validation of the experimental setup (see Material and Methods), we next tested how
319 His-MinC and His-PDZ affect MinD-liposome binding kinetics by subjecting a liposome coated

320 sensors to solutions containing 8 µM His-MinD and varying concentrations [1, 2, 4, 8 and 16
321 µM] of His-MinC or His-PDZ, respectively (Fig. S 11, Tab. 2). MinD controls appear twice in
322 the table, because the experiments were performed using two independent purification
323 batches. The corresponding His-MinC and His-PDZ samples were each paired with the His-
324 MinD batch they contained. Due to batch-specific differences in His-MinD stability and
325 degradation, we did not directly compare measurements across batches. Interestingly,
326 neither His-MinC nor the His-PDZ domain significantly altered the membrane binding
327 kinetics of His-MinD in BLI experiments. The extracted K_D, k_{on}, and k_{off} values differed only
328 marginally between conditions (Tab. 2**Error! Reference source not found.**), and these
329 apparent shifts fell within the fitting uncertainty and typical inter-run variability of BLI. This
330 contrasts with the slight increase in His-MinD ATPase activity observed in the presence of
331 His-PDZ (Fig. S 5), which had led to the hypothesis that PDZ might promote MinD
332 oligomerization at the membrane, enhancing ATP hydrolysis. However, the discrepancy
333 between the two systems and the high lipid concentration (2 mg/ml) in the ATPase assay
334 versus a liposome-coated sensor in BLI may account for the different outcomes. In the BLI
335 experiment, limited surface area and distinct spatial organization of liposomes may restrict
336 the ability of the soluble PDZ domain to effectively cluster MinD, unlike full-length MinJ,
337 which is membrane-anchored via its transmembrane helices. Thus, while the PDZ domain
338 alone appears insufficient to modulate membrane binding kinetics of MinD, it remains
339 plausible that the full-length MinJ could exert a more pronounced effect through spatial
340 coordination at the membrane.

341 **Single-molecule localization microscopy confirms *in vitro* data.**

342 To validate the biochemical *in vitro* results, we decided to utilize single-molecule localization
343 microscopy (SMLM) with focus on single-molecule tracking (SMT), a technique allowing to

344 observe and evaluate MinD dynamics *in vivo* inside *B. subtilis* cells. We began SMLM analysis
345 by plotting a heat-map of the intracellular localization of all individually recorded Halo-MinD
346 molecules as well as the mutated variants, respectively, on normalized cells (Fig. 4 A). This
347 representation did not only provide a robust internal control for the imaging and post-
348 processing process for the well characterized localization of MinD, but also revealed
349 systemic differences in localization caused by the respective mutations. The first obvious
350 difference is reduced MinD enrichment at the cell center and poles in the G12V or K16A
351 variants. (Fig. 4 A). Here, the membrane-bound MinD fraction seems to be much more
352 evenly distributed along the membrane, similar to what we observed during wide-field
353 microscopy (Fig. 2 B). This result does not only confirm the ability of MinD monomers to bind
354 the membrane (Fig. 3 C & D), but also fuels the speculation that MinJ might be unable to
355 recruit MinD in its monomeric form, so that polar and septal recruitment by MinJ requires
356 dimeric MinD. In combination with the information obtained from BLI results (Fig. 3), this
357 could mean that the membrane itself serves as proxy for MinD dimerisation and subsequent
358 recruitment, quickly followed by ATP hydrolysis and membrane detachment of MinD. In
359 contrast, but in agreement with wide-field imaging (Fig. 2 B), the Halo-MinD-D40A mutant
360 does appear to frequently form foci and larger local accumulations, with little protein in the
361 cytosolic fraction (Fig. 4 A). This, again, could be caused by local MinJ interaction and
362 recruitment in combination with the missing capability of membrane detachment or with
363 increased lateral MinD interactions (73). Finally, the I260E mutant appears evenly distributed
364 throughout the cell (Fig. 4 A), as it was expected.

365 Independently, all protein trajectories were subjected to a stationary localization analysis
366 (SLA) (Fig. 4 B). This was done by first grouping all trajectories into an either mobile or static
367 population by testing if the molecule left a circle with a diameter of 97 nm (equaling the

368 pixel size of the imaging setup) within at least five consecutive frames. Trajectories that were
369 classified as mobile were further sub-grouped into mixed and free trajectories, where only
370 free trajectories never presented a confinement event (74). In agreement with previous
371 data, the D40A mutant displayed the highest fraction of static tracks (Fig. 4 B), and by far the
372 lowest proportion of truly free trajectories (48.5 %). In contrast, more than 90% of Halo-
373 MinD-I260E molecules were classified as free with only few trajectories classifying as static
374 (Fig. 4 B), accentuating the absence of interaction with the membrane or other structures.
375 When comparing Halo-MinD to the monomeric mutants G12V and K16A, the number of
376 static tracks was visibly reduced in the mutants. Since both monomers are unable to
377 dimerise, it is less likely that they can form larger clusters, which we observed in a previous
378 study (61). Between both monomeric mutants, K16A displayed a slightly larger number of
379 static trajectories (Fig. 4 B), which is in alignment with BLI data, where the K16A mutant
380 dissociates much less effective from the membrane (Fig. 2 C & D, Tab. 1**Error! Reference**
381 **source not found.**).

382 Next, we examined the average intracellular mobility of Halo-MinD compared with the
383 mutant variants by analyzing the mean-squared displacement (MSD, Fig. 4 C). In MSD
384 analysis, the traveled distances of recorded trajectories are plotted against a given time lag
385 (Δt) as a function of Δt, here one imaging frame (24 ms), where the slope can indicate the
386 speed (75-77). As expected, the I260E mutant displayed the fastest average mobility, since it
387 does not bind the membrane effectively anymore (Fig. 4 C). In contrast, the D40A mutant
388 was the slowest recorded protein, indicated by the only mild incline (Fig. 4 C). Since we
389 expect most of the proteins' population to be membrane bound, and furthermore observed
390 larger foci that suggest cluster formation, this was expected. Halo-MinD wild type protein
391 appeared to be more mobile in comparison (Fig. 4 C), as it should exist in both monomeric

392 and dimeric conformation and either freely diffusive in the cytosol or interact with the
393 membrane. Last, the two monomeric mutants G12V and K16A displayed extremely similar
394 average speeds that were both faster than the wild type protein (Fig. 4 C). Since these MinD
395 variants cannot form dimers, general diffusion should be faster, as there should be no MinD
396 dimers or oligomers, and possibly no recruitment by MinJ.

397 If the underlying movement in MSD analysis can be described by simple Brownian motion,
398 the gradient of the curve is proportional to the diffusion coefficient *D* (77). We know,
399 however, that MinD interacts at least with MinC, MinJ, the membrane and itself, in
400 combination with the fact that bacterial cells exhibit natural confinement. With these
401 information one cannot assume simple Brownian motion, therefore we have chosen jump
402 distance (JD) analysis as a more accurate assessment to describe Halo-MinD dynamics (Fig. 4
403 D & E). In JD analysis, the distances molecules travel between subsequent frames are plotted
404 in a probability distribution (Fig. 4 E), and diffusion coefficients are obtained by curve fitting
405 (77), in this case with a three-component model separating fast, slow and confined
406 molecules (Fig. 4 D & E). To accurately compare population sizes, the simultaneous option
407 was chosen in the SMTracker software, fixing the diffusion coefficients for every MinD
408 variant (74). To also obtain individual, variant specific diffusion coefficients, the same data
409 was additionally fitted individually (non-simultaneous SQD analysis in SMTracker2, Tab.
410 3**Error! Reference source not found.**).

411 Generally, the results of JD analysis correlated well with our *in vitro* data. When dissecting
412 the different populations in the wild type, more than a third of all proteins appear to be
413 confined (36.6%, Fig. 4 D), which likely comprises membrane bound protein that is further
414 stabilized by protein-protein interactions via lateral interaction of MinD with itself, and
415 possibly MinC and MinJ. The slow mobile population was the largest (45.7%, Fig. 4 D), and

416 likely summarizes different conformations of MinD that interact with the membrane, but are
417 still diffusive and not captured or stabilized through further interactions. The third, fast
418 diffusive population (17.7%, Fig. 4 D) likely reflects cytosolic MinD. These results stress the
419 importance of the MinD ATPase cycle for its localization and dynamics, as these are severely
420 altered in the MinD mutants.

421 In detail, the probability distributions of Halo-MinD-D40A and I260E (Fig. 4 E) illustrate the
422 strong shift between MinD molecules in a confined (D40A) and a diffusive state (I260E) best.
423 When examining the different populations, most Halo-MinD-D40A molecules were classified
424 as confined (54.2%) and slow mobile (40.2%), whereas I260E only displayed ~9% of confined
425 molecules (Fig. 4 D), matching prior results and expectations of the membrane binding
426 mutant. When comparing D40A to wild type Halo-MinD, the largest shift is observed
427 between the fast mobile and confined populations, shifting towards a distinctively more
428 confined regiment in the D40A mutant (36.6% WT, 52.2% D40A; Fig. 4 D) and visible
429 disappearance of the fast population in the probability distribution (Fig. 4 E). These results
430 are in line with the previous observations, as a trapped dimer of MinD will remain at the
431 membrane at much higher efficiency (Fig. 3 E & Tab. 1**Error! Reference source not found.**),
432 and appeared to form foci and clusters (Fig. 2 B, Fig. 4 A). G12V and K16A mutants on the
433 other hand showed an increase in fast mobile populations (WT 17.7%, G12V 25.8%, K16A
434 26.6%; Fig. 4 D E), which could be attributed to a reduced interaction with MinD interaction
435 partners (MinC, MinD, MinJ and plasma membrane). This notion is supported by the
436 decrease in confined molecules for both G12V and K16A mutants compared to the wild type
437 (WT 36.6%, G12V 23.7%, K16A 29%; Fig. 4 D & E), which are expected to be membrane
438 bound and likely stabilized through other protein-protein interaction, which may be reduced
439 or absent in the monomeric conformation. This notion is also supported by the absence of a

440 MinD gradient in epifluorescence images of G12V and K16A mutants (Fig. 2 B), a pattern
441 usually formed through sequestering via MinJ. Finally, when comparing both monomeric
442 variants, the K16A mutant displays a noticeable shift between the slow diffusive (G12V
443 50.5%, K16A 44.3%; Fig. 4 D) and confined populations (23.7% G12V, 29% K16A; Fig. 4 D).
444 The larger confined population of Halo-MinD-K16A is consistent with the BLI results (Fig. 3 D,
445 Tab. 1**Error! Reference source not found.**), where K16A appears to have a lower dissociation
446 from the membrane, increasing its likelihood of confinement, possibly caused by the inability
447 to bind ATP.

448 In summary, these results emphasize the importance of the MinD ATPase cycle for
449 functionality of the Min system in *B. subtilis*. Even though *B. subtilis* MinD is not capable of
450 oscillation, its intracellular dynamics are highly dependent on the functionality of the MinD
451 ATPase domain and its catalytic site, which is reflected by the variety of localization and
452 interaction defects displayed by the MinD mutants on a molecular level, that all result in
453 severe division anomalies.

454 **MinC and MinJ have different effects on MinD protein dynamics in SMLM.**

455 MinC and MinJ interact with MinD *in vivo*, suggesting protein dynamics should be affected
456 by this. However, in our ATPase and BLI experiments, MinC had only minor effects on ATPase
457 activity and membrane binding kinetics of MinD, while the PDZ domain slightly enhanced
458 ATPase activity without altering membrane binding kinetics of MinD. To validate these
459 observations *in vivo* and to identify differences between MinD interacting with a cytosolic
460 PDZ-domain or a full-length MinJ, we performed the same SMLM workflow and analysis
461 pipeline described in the previous section on cells expressing Halo-MinD in Δ*minC* and Δ*minJ*
462 backgrounds and compared them to the wild type background (Fig. S 12, Tab. 4).

463 When comparing the average Halo-MinD distribution between the respective strains, the
464 Δ*minC* mutant exhibited a similar intracellular localization pattern as the wild type, with
465 strong membrane enrichment and highest concentrations at midcell and poles (Fig. S 12 A).
466 However, Δ*minC* cells interestingly exhibited a slightly reduced cytosolic signal and a
467 corresponding increased membrane association. As expected, Δ*minJ* cells lacked the
468 characteristic septal accumulation. Instead, Halo-MinD was distributed relatively uniformly
469 along the membrane, consistent with MinJ being required for efficient sequestering of MinD
470 to the future division site and cell poles.

471 In the stationary localization analysis (Fig. S 12 B), Halo-MinD in the Δ*minC* strain displayed
472 only a modest increase in the static fraction compared to wild type (23.4 % from 20.1 %).
473 This shift can be attributed to a reduction in the mixed, likely membrane-interacting
474 population (from 19.0 % to 14.7 %), whereas the freely mobile fraction remained essentially
475 unchanged (61 % to 62 %). These results indicate that in the absence of MinC, less MinD
476 moves along the membrane and a slightly larger proportion becomes immobilized. Although
477 the effect size is small, it suggests that MinD may form larger or slightly more stable
478 membrane-associated assemblies when MinC is absent *in vivo*. In the Δ*minJ* background, the
479 static Halo-MinD population surprisingly increased (20.1 % to 28.2 %), together with
480 respective reductions in both the freely diffusing cytosolic pool (61.0 % to 56.6 %) and the
481 mixed, likely membrane-interacting population (19.0 % to 15.1 %). This redistribution
482 suggests that MinJ contributes to efficient MinD turnover on the membrane, in line with
483 MinD ATPase data with His-PDZ (Fig. S 12). In the absence of MinJ, MinD appears to remain
484 membrane-bound for longer, consistent with impaired detachment or reduced cycling
485 between membrane-associated states. One possible explanation is that MinD may form
486 more stable or aggregation-prone assemblies when MinJ is absent, whereas the presence of

487 MinJ could promote more dynamic membrane association and hence sharper local
488 accumulations and cycling of MinD, necessary for enriched polar and septal localization.
489 Jump-distance analysis with fixed diffusion coefficients corroborated these findings (Fig. S 12
490 C & D), showing that Δ*minJ* cells contained a substantially enlarged confined population of
491 MinD (27.9 % vs. 44.9 %), together with a large reduction of the slow diffusive population
492 (50.9 % vs. 37.8 %). Fitting the data without fixed diffusion coefficients produced the same
493 trend (Tab. 4), indicating that the shift reflects MinD spending more time in the respective
494 state rather than actual changes in the underlying diffusive coefficients.

495 In the Δ*minC* strain, Halo-MinD shows a slight redistribution toward the confined state, with
496 an increased fraction of very slow or immobile molecules (27.9 % vs. 36.8 %) and a
497 corresponding decrease in both the fast and intermediate populations (50.9 % vs. 45.8 % and
498 21.2 % vs. 17.4 %, respectively, Fig. S 12 C & D). SQD analysis without fixed diffusion
499 coefficient (Tab. 4) shows that the diffusion coefficients of the fast and intermediate
500 populations are reduced compared with wild-type, indicating that the mobile molecules
501 themselves move more slowly in average. Combined, this could suggest that in the absence
502 of MinC, membrane-bound MinD is more prone to forming clusters or larger aggregates,
503 which restrict mobility and reduce the efficiency of its membrane cycling.

504 Together, these data suggest that MinJ promotes productive membrane cycling of MinD,
505 and in its absence, MinD accumulates more often in a confined, likely non-productive
506 membrane-associated state, whereas MinC plays a comparatively minor regulatory role,
507 where it passively contributes to MinD mobility by preventing excessive clustering and
508 facilitating proper membrane-associated dynamics.

Discussion

In bacteria, the oscillation of MinCDE in *E. coli* is one of the best studied examples of a reaction-diffusion system, and the two core components MinD and MinE cycle between membrane and cytosol in an ATP-dependent manner, generating a standing wave with a time-resolved minimum at midcell (15, 83). Here, binding and unbinding of the components to the membrane surface influences the diffusion coefficients and controls the dynamic activity of MinC (84). While the *E. coli* MinCDE system is one of the best-studied examples of intracellular pattern formation in bacteria (15, 84-86), the Min system in *B. subtilis* remains less well characterized. In a previous study (61), we suggested that gradient formation depends on ATPase-driven MinD dynamics, backed by PALM and FRAP analysis as a basis for a mathematical model. However, due to a lack of biochemical data, we had to assume that the *B. subtilis* MinD cycles between membrane-bound and cytosolic localizations based on ATP-binding and hydrolysis, similar to *E. coli* MinD (61). A further gap in our knowledge of the *B. subtilis* Min system concerned the activation mechanism of MinD in absence of a MinE homolog.

To address this gap, we first analyzed *B. subtilis* MinD biochemically *in vitro*. Purified MinD showed basal ATPase activity that drastically increased upon liposome addition. Although *E. coli* MinD similarly requires lipids, it additionally depends on MinE for full activation (64). The reported maximum ATPase rate, around 20 nmol mg^{-1} min^{-1} (64, 65), was nearly identical to that of *B. subtilis* MinD, indicating that membrane binding alone is sufficient to trigger robust ATP hydrolysis in the *Bacillus* system. When comparing to other MinD/ParA ATPases that have been biochemically characterized, the activity level of *B subtilis* MinD is on the lower end of the spectrum with a k_{cat} of 36.27 h^{-1}. Soj, the ParA homologue in *B. subtilis*, reaches

533 more than 2-fold higher catalytic activity (83.6 h^{-1}) when fully activated by supplementing
534 Spo0J (ParB) and DNA (87), similarly to Soj in *Thermus thermophiles* combined with Spo0J
535 and *parS* containing DNA (70). Studies investigating the activity levels of ParA in *Caulobacter*
536 *crescentus*, purified in presence of ATP, determined a k_{cat} of 0.79 min^{-1} (47.4 h^{-1}) in absence
537 of ParB, increasing almost 5-fold to 3.7 min^{-1} (222 h^{-1}) in presence of ParB (88). A more
538 recent study found the *C. crescentus* ParA k_{cat} increase from 5.8 hr^{-1} to 120 hr^{-1} upon
539 addition of ParB (89).

540 These findings suggest that membrane association is the primary trigger for MinD ATPase
541 activity in *B. subtilis*. Specifically, the comparison of maximum velocities, activity stimulation
542 factors, and K_M values between the *E. coli* and *B. subtilis* MinD proteins suggests that a
543 functional homolog of the MinE protein is not necessary in *B. subtilis*. At the same time, our
544 biochemical data indicate that MinJ/PDZ increases MinD ATP hydrolysis rates at least to a
545 modest extent, (between 22% and 37%, Fig. S 5 B), pointing to a broader regulatory
546 influence of MinJ on MinD that becomes evident from additional mechanistic analyses
547 discussed below. In contrast, the presence of MinC led only to a slight decrease in MinD
548 ATPase activity in our APTase assays (~ 5%, Fig. S 5 A). This modest inhibitory effect suggests
549 that MinC does neither directly stimulate MinD turnover nor inhibit it, and may instead
550 stabilize MinD in a conformation or assembly state with mildly reduced catalytic activity, also
551 discussed below.

552 With the goal of testing binding of isolated MinD to the membrane, we designed a Bio-layer
553 interferometry experiment in which we immobilized liposomes and measured binding of
554 purified MinD proteins. Importantly, without addition of ATP (and ADP present from
555 purification) we observed only very weak MinD binding to the liposomes (Fig. S 13),
556 indicating that MinD membrane binding and dissociation is coupled to the ATP hydrolysis

557 cycle or the nucleotide binding state. In presence of ATP, MinD readily binds to the
558 liposomes with high affinity. The ParA/MinD family is well studied, and mutations producing
559 strictly monomeric (G12V, K16A), dimeric (D40A), or membrane-binding-deficient (I260E)
560 MinD variants are well established (68-70). The most intriguing observation of the binding
561 experiments is that MinD monomers can apparently bind to the liposome membrane *in*
562 *vitro*. Both monomeric mutants (G12V and K16A) are readily binding to the membrane, but
563 the release of the proteins from the membrane surface differs drastically. While the K16A
564 mutant, unable to bind ATP, has a slow membrane release rate (k_{off} rate of only $2.77*10^{-3}$ s^{-}
565 ^{1}), the G12V monomeric mutant, which can still bind ATP, is released fast from the
566 membrane (k_{off} rate $47.8*10^{-3}$ s^{-1}). The D40A mutant of MinD, which is thought to be a stable
567 ATP-bound dimer, releases with very slow kinetics (k_{off} rate $1.76*10^{-3}$ s^{-1}). This indicates that
568 ATP hydrolysis accelerates MinD release from the membrane and that ATP binding itself
569 influences MinD association and dissociation kinetics, although we cannot entirely exclude
570 that the mutations introduce subtle structural changes that affect membrane affinity. These
571 findings crucially support a reaction diffusion model in which the MinD ATPase cycle is
572 essential for correct pattern formation of *B. subtilis* MinD. When testing the impact of MinC
573 on MinD membrane-binding kinetics, no significant differences were observed, suggesting
574 that MinC does not substantially influence the binding dynamics of MinD, in-line with the
575 collective view of MinC as a passenger rather than a driver of MinD dynamics (84). It would
576 have been desirable to study the interaction of MinD with reconstituted full-length MinJ
577 proteins to specifically investigate the influence that MinJ has on membrane interaction of
578 MinD. Unfortunately, we did not succeed in the purification of a full length MinJ protein so
579 far. MinJ contains seven predicted transmembrane helices and displays a pronounced
580 instability, rendering purification difficult. While the binding kinetics were unaffected during

581 BLI, our *in vitro* ATPase experiments combining the soluble PDZ domain of MinJ with MinD
582 already demonstrate that MinJ possibly modulates MinD:membrane interactions to some
583 extent through an effect on the hydrolysis efficiency.

584 To clarify this point and to better understand the isolated MinD membrane interaction under
585 *in vivo* conditions, we turned to state-of-the-art microscopy (SMLM) (92, 93).

586 SMLM data comparing the behavior of MinD in wild type vs. Δ*minJ* background (Fig. S 12)
587 collectively suggest that MinJ stabilizes correct pattern formation of MinD. By promoting
588 efficient membrane detachment and maintaining MinD in a dynamically cycling state, MinJ
589 appears to ensure that MinD remains properly redistributed throughout the cell cycle rather
590 than becoming sequestered in non-productive clusters. This organizational role likely
591 underlies the ability of MinJ to position MinD, and thus MinC, at the appropriate cellular
592 sites (55, 56), thereby supporting robust spatial regulation of division. However, a short-lived
593 MinJ mediated stabilization of MinD-dimers at the membrane would be comparable to the
594 stabilizing effect that MinE has on MinD oligomers in *E. coli* (90, 91), and was previously
595 observed in our *in vivo* FRAP studies (61). In contrast to MinJ, MinC did not seem to have a
596 major impact on MinD dynamics *in vivo*. When observing MinD in absence of *minC*, the main
597 effect was a subtle reduction in MinD cycling activity, shifting a small fraction of MinD into
598 more static or confined membrane-associated states. In the wild type situation, MinC may
599 passively restrict uncontrolled aggregation by capping or destabilizing certain interfaces, or
600 conversely transiently stabilize short-lived assemblies required for regulation.

601 The locked MinD dimers (D40A mutant) frequently nucleated into larger membrane clusters.
602 This cluster formation is underlined by the drastic increase of the confined/immobile
603 population (54.2%) of D40A in SMLM. This increase in the static population comes to the

604 expense of freely diffusive protein (~5.6 %), indicating that the vast majority of MinD D40A is
605 membrane associated. We observed a clear enrichment of these MinD clusters at the cell
606 poles and septa, lending support to the notion that MinD dimers are specifically
607 stabilized/recruited by MinJ. This interpretation is supported by previous data showing that
608 in absence of MinJ, MinD proteins are randomly localized along the membrane in clusters,
609 but not enriched at poles or (in a *minJ* mutant background rare) septa (57). In line with this
610 idea, the monomeric MinD variants (G12V, K16A) are evenly bound to the membrane
611 surface along the entire cell length.

612 The fact that most monomeric MinD appears membrane associated *in vivo* also supports our
613 *in vitro* measurements in which monomeric MinD variants efficiently bind the membrane, a
614 notion strongly supported by a recent report that examined localization of the same
615 monomeric variants in epifluorescence microscopy (94). The time-resolved MinD gradient is
616 lost in all mutants - including D40A - which should still be recruited by MinJ, suggesting the
617 ATPase cycle and thus MinD cycling is indeed necessary for proper formation of a gradient,
618 as suggested before (61). Our data are in perfect agreement with recent *in vitro* data
619 collected with the *E. coli* MinD using mass-sensitive particle tracking (MSPT) (73). MSPT
620 analysis revealed that *E. coli* MinD forms lateral interactions, leading to higher order
621 oligomers (trimer, tetramer and even higher oligomers). It was speculated that dimerization
622 of *E. coli* MinD at the membrane leads to conformational changes opening an additional
623 interaction surface of MinD for lateral interaction (73). These lateral MinD interactions were
624 thought to recruit further monomeric MinD from solution to the membrane, thereby
625 forming a nucleation for larger clusters. The MinD cluster formation that we observed in *B.*
626 *subtilis* using SMLM (61) are likely *in vivo* evidence for this cooperative membrane binding. It
627 should be noted that the MSPT analysis was not sensitive enough to detect monomer

628 binding to the membrane, but this was explicitly not ruled out (73). Addition of a second
629 amphipathic helix to the *E. coli* MinD however, was shown to promote monomer binding of
630 *E. coli* MinD to the membrane (66). Thus, the difference between the *E. coli* and *B. subtilis*
631 MinD is likely the higher membrane binding capacity of the *Bacillus* protein. The observed
632 cooperativity in membrane binding and thus nucleation, as shown for the *E. coli* MinD in
633 vitro (66, 73) and here for the *B. subtilis* MinD *in vitro* and *in vivo*, is required for pattern
634 formation by conferring nonlinearity (61, 95, 96).

635 Consistent with this model, our SMT data revealed three major dynamic states of MinD: fast
636 cytosolic diffusion, a slower membrane-associated pool, and a confined fraction
637 corresponding to clustered or multimeric assemblies. Most of the membrane-binding-
638 deficient mutant I260A shifted drastically into the fast, cytosolic population, validating this
639 assignment. Conversely, the locked-dimer (D40A) mutant showed a pronounced increase in
640 confined, slow-moving molecules, in line with its strong tendency to nucleate clusters.
641 Monomeric variants (G12V, K16A) displayed reduced confinement, supporting the view that
642 dimerization is required for higher-order assembly or recruitment. Together, these
643 observations indicate that MinD dynamically cycles between cytosol and membrane in an
644 ATP-dependent manner. Thus, we conclude that membrane bound dimers of MinD have a
645 much stronger tendency to interact with and recruit binding partners (including self-
646 nucleation). This finding is further supported by a recent report that analyzed MinD
647 dynamics *in vivo* using diffraction limited microscopy (94). In this study, a MinD D40A mutant
648 hyper-recruited MinC, leading to cluster formation of MinCD at the membrane. Deletion of
649 MinC restored the MinD gradient formation, indicating that MinC might indeed be part of a
650 MinC:MinD co-polymer, as suggested for the *E. coli* system (97). This assumption is in good
651 agreement with our *in vivo* findings, where self-nucleation seems to increase drastically for

652 the D40A mutant or in absence of MinJ. In contrast, monomeric G12V and K16A mutants do
653 not display this behavior, in line with monomeric MinD variants not being able to interact
654 with MinC, which was similarly observed through widefield microscopy in the same study
655 (94).

656 Collectively, our data reveal that the MinD ATPase cycle is essential for regulated membrane
657 binding and release, which is crucial for the formation of a sharp MinD gradient at the
658 septum (61). However, in contrast to *E. coli* MinD, monomeric *B. subtilis* MinD can bind the
659 membrane with higher affinity, suggesting that MinD also dimerizes at the membrane
660 surface. Dimer formation is essential for ATPase activity, as indicated by our *in vitro*
661 measurements, and is necessary for efficient membrane detachment. The main
662 characteristics of the *E. coli* MinD with respect to membrane binding, self-interaction leading
663 to nucleation, and membrane detachment are therefore shared in the *B. subtilis* protein. The
664 difference, that ATP hydrolysis of the *B. subtilis* MinD does not require a trigger other than
665 membrane binding, makes sense in a system that does not need to oscillate, but rather
666 accumulate and sustain a sharp gradient at the current site of division. However, the balance
667 of a dynamic membrane cycle of MinD seems to be fine-tuned by the interaction with MinC
668 and especially MinJ, which appears to keep MinD in a productive state and protects it from
669 aberrant aggregation, while recruiting it towards poles and septum, the intended site of
670 action of MinC.

671

Materials and Methods

Bacterial strains, plasmids and oligonucleotides

Plasmid and strain construction of all relevant constructs is described in the supplementary information. Oligonucleotides, plasmids and strains used in this study are listed in Tab. S 2, Tab. S 3 and Tab. S 4, respectively.

Media and growth conditions

E. coli was grown on lysogeny broth (LB) agar plates containing 10 g L^{-1} tryptone, 5 g L^{-1} yeast extract, 10 g L^{-1} NaCl and 1.5% (w/v) agar at 37°C overnight using appropriate selection (kanamycin 50 µg ml^{-1}, chloramphenicol 35 µg ml^{-1}).

B. subtilis was grown on nutrient agar plates using commercial nutrient broth and 1.5% (w/v) agar at 37°C overnight. To reduce inhibitory effects, antibiotics were only used for transformations and when indicated, since allelic replacement is stable after integration (kanamycin 5 µg ml^{-1}, spectinomycin 100 µg ml^{-1}).

For microscopy, *B. subtilis* was inoculated to an OD_{600} 0.05 from a fresh overnight culture and grown in MD medium - a modified version of Spizizen Minimal Medium (98) – at 37°C with aeration in baffled shaking flasks (200 rpm) to OD_{600} 0.5-0.8. MD medium contains 10.7 mg ml^{-1} K_2HPO_4, 6 mg ml^{-1} KH_2PO_4, 1 mg ml^{-1} Na_3 citrate, 20 mg ml^{-1} glucose, 50 µg ml^{-1} L-tryptophan, 11 µg ml^{-1} ferric ammonium citrate, 2.5 mg ml^{-1} L-aspartate and 0.36 mg ml^{-1} $MgSO_4$ and was always supplemented with 1 mg ml^{-1} casamino acids. Subsequently, cultures were diluted to OD_{600} 0.05 in fresh, pre-warmed MD medium and grown to OD_{600} 0.5 (exponential phase).

Purification of His-MinC, His-PDZ, His-MinD and variants

695 For heterologous expression of His-MinC, His-PDZ and His-MinD and its variants, freshly
696 transformed BL21(DE3) cells carrying the respective pET-28a expression vector (Tab. S 3) as
697 well as pLysS (His-MinC, His MinD and variants only) were transferred to LB medium with
698 appropriate selection (kanamycin 50 µg ml^{-1}; chloramphenicol 35 µg ml^{-1} in presence of
699 pLysS) and grown overnight (37°C, 200 rpm). The next day, fresh LB medium was inoculated
700 1:150 from the overnight culture and grown to an OD_{600} of 0.5 at 37 °C and 200 rpm. Since
701 His-PDZ tended to form inclusion bodies under these conditions, its expression culture was
702 instead grown at 18 °C and 120 rpm without IPTG induction. For all other constructs, protein
703 expression was induced with 1 mM IPTG. Cells expressing His-MinC and all His-MinD variants
704 were harvested after 3 h of induction, whereas His-PDZ cultures were collected after
705 overnight incubation. Cells were harvested by centrifugation (4 °C, 5000 × g, 15 min) and
706 stored at -80°C. For purification, a protocol of *E. coli* MinD purification was adapted from
707 (63): the cell pellet was resuspended on ice in lysis buffer (50 mM NaH_2PO_4, 500 mM NaCl
708 and 10 mM imidazole; pH 8.0), supplemented with protease inhibitor cocktail (Roche), 0.2
709 mM Mg^{2+}-ADP and 0.4 mM TCEP (His-MinD and variants only) and ~250 U mL^{-1} DNase I
710 (Roche), and subsequently lysed in a pre-cooled (4°C) French pressure cell (Amico; 3 x 1,200
711 psi). The debris was then removed via centrifugation (10,000 g, 30 min, 4°C) and the
712 supernatant was passed through a 1 ml Ni-NTA column (Protino, Macherey-Nagel) utilizing
713 liquid chromatography (ÄKTApurifier). Here, the resin was washed with 10 ml binding buffer
714 A (50 mM NaH_2PO_4, 500 mM NaCl, 20 mM imidazol; pH 8) before elution buffer B (50 mM
715 NaH_2PO_4, 500 mM NaCl, 250 mM imidazol; pH 8, (and 0.2 mM Mg^{2+}-ADP and 0.4 mM TCEP
716 for His-MinD and variants)) was added sequentially at concentrations of 5% (10 ml) 10% (20
717 ml), and finally 100% (10 ml). Recombinant protein eluate was collected in 0.5 ml fractions.
718 Fractions containing high concentrations of protein (determined by chromatogram analysis,

719 sodium dodecyl-sulfate polyacrylamide gel electrophoresis (SDS-PAGE) and Western blotting
720 using Penta-His antibody (QIAGEN)) were pooled and concentrated using Amicon filter
721 devices with 10 kDa molecular weight cut-off (Millipore; Merck). Additionally, protein
722 aggregates were removed by pelleting them through centrifugation (10,000 g, 10 min, 4°C).

723 Samples were further purified by size-exclusion chromatography through a Superdex200
724 Increase 10/300 GL column (Cytiva) at a flow rate of 0.75 ml min^{-1} using gel filtration buffer C
725 (50 mM HEPES-KOH, 150 mM KCl, 10% (v/v) glycerol, 0.1 mM EDTA, pH 7.2). For His-MinD
726 and its variants, buffer C was supplemented with 0.4 mM TCEP and 0.2 mM Mg^{2+}-ADP
727 immediately before use. His-PDZ was not subjected to size-exclusion chromatography
728 because it could not be recovered after SEC. Instead, it was used directly following affinity
729 purification. To calibrate the column and allow identification of relevant fractions, a gel
730 filtration standard (Bio-Rad) was run according to the manufacturers protocol and analyzed
731 using the same conditions, respectively. Fractions containing recombinant protein were
732 pooled and either directly used for the respective assays, stored at 4°C for a maximum of
733 one week or flash-frozen and stored at -80 °C. Final protein concentration was determined
734 using Bradford assay with bovine serum albumin (BSA) as standards. Protein purity and
735 stability was confirmed via SDS-PAGE using 12% polyacrylamide gels and Western blotting
736 using Penta-His antibody (QIAGEN) (Fig. S 1, Fig. S 3, Fig. S 4, Fig. S 6 Fig. S 8, Fig. S 9 and Fig.
737 S 10).

738 **ATP hydrolysis assays**

739 ATP hydrolysis was analyzed in continuous reactions using the EnzChek Phosphate Assay Kit
740 (Thermo Fisher Scientific), according to the manufacturer's manual. Reaction volumes were
741 reduced to 100 µl and assayed in flatbottom 96-well plates (Greiner-UV-Star 96-well plates).

742 Reactions were measured at 37 °C continuously every minute over a time-course of 3 h in a
743 Tecan Infinite 200 Pro with the Software Tecan i-control v.2.0. If not indicated differently,
744 the reactions contained either 0-16 µM His-MinD or the respective variant/protein
745 combination as well as 2 mM Mg^{2+}-ATP and 0.2 mg ml^{-1} liposomes. Liposomes were made
746 from *E. coli* total extract (Avanti) by first drying and then resuspending and rehydrating lipids
747 in gel filtration buffer C (50 mM HEPES-KOH, 150 mM KCl, 10% (v/v) glycerol, 0.1 mM EDTA).
748 Next, the lipids were extruded 40 times through 100 nm polycarbonate membranes
749 (Nuclepore™ Track-Etched Membrane 0.1 µm, Whatman). Before starting the reactions with
750 2 mM Mg^{2+}-ATP, the plate was preincubated for 10 min in order to eliminate phosphate
751 contamination.

752 Data were first analyzed with Excel (normalized, subtraction of ATP auto hydrolysis and
753 subtraction of no substrate control), a linear regression was used to determine the
754 hydrolysis rate per minute. Data visualization and further analysis was performed using
755 GraphPad Prism version 9.4.0 for Windows, (GraphPad Software). Statistical comparisons
756 between His-MinD alone (n = 2) and His-MinC/His-PDZ conditions (n = 3 each) were
757 performed using Welch's t-test (two-tailed), which is appropriate for unequal variances and
758 unequal sample sizes.

759 **AlphaFold prediction and structure-based analysis**

760 A structural model of *B. subtilis* MinD was calculated using AlphaFold2 (99) installed on a
761 local computer (Fig. 2 A), where the structural homology search was performed against the
762 full AlphaFold database as of 11.02.2024 (99).

763 A structural model of *B. subtilis* MinJ was calculated using AlphaFold3 (100), where the
764 structural homology search was performed against the full AlphaFold database as of
765 01.02.2025 (100).

766 **Bio-layer Interferometry**

767 Measurements were performed on the BLItz platform (Sartorius) using Streptavidin (SA)
768 Biosensors (Sartorius, 18-5019). The BLItz device was operated with the Software BLItz Pro
769 (version 1.3.1.3) using the advanced kinetics protocol modified as shown in Table S5 and
770 essentially as described before (101-103).

771 Beforehand, Liposomes were made from a 33:1 mixture of *E. coli* total extract (Avanti) and
772 DSPE-PEG$_{(2000)}$-biotin (Avanti) by first drying and then resuspending and rehydrating lipids in
773 gel filtration buffer C (50 mM HEPES-KOH, 150 mM KCl, 10% (v/v) glycerol, 0.1 mM EDTA).
774 Next, the lipids were extruded 40 times through 100 nm polycarbonate membranes
775 (Nuclepore™ Track-Etched Membrane 0.1 µm, Whatman). Biosensors were hydrated for at
776 least 10 min in a 96-well plate in 200 µl gel filtration buffer C.

777 As a starting point, unspecific binding was tested. For this, non-biotinylated His-MinD was
778 used to be loaded onto the Streptavidin biosensor. For the binding assays, all measurements
779 were performed in black reaction tubes with 200 µl gel filtration buffer C or the indicated
780 solution (Tab. S 5). After measuring the initial baseline, biotinylated liposomes were allowed
781 to bind the biosensor. Another baseline was measured in the same tube as before. For
782 association, 200 µl solutions of His-MinD and variants in different concentrations and/or in
783 combination with His-MinC or His-PDZ, respectively, were exposed to the sensor, first
784 without and later with addition of 2 mM Mg-$^{2+}$ATP (final concentration) just before use.
785 Furthermore, unspecific binding to liposome-saturated sensors was tested using bovine

786 serum albumin (BSA, 16 µM). For dissociation, the sensor was exposed to buffer again. Each
787 measurement was performed with a fresh biosensor.

788 For BLI experiments involving His-MinD and one of its direct interactors, we first assessed
789 whether His-MinC or His-PDZ can directly interact with His-MinD *in vitro*. To this end, a
790 liposome-coated BLI sensor was first dipped into a 8 µM His-MinD solution. Subsequently,
791 the sensor was exposed to solutions containing either 8 µM His-MinD together with 8 µM
792 His-MinC or 8 µM His-PDZ, respectively. As a negative control, a sample containing 8 µM
793 His-MinD and 8 µM BSA was used. Both His-MinC and His-PDZ induced a significant increase
794 in the equilibrium binding signal upon interaction with immobilized His-MinD, consistent
795 with specific complex formation. In contrast, the BSA control showed only a minimal signal
796 increase, confirming the specificity of the observed binding. To further validate the sensor
797 specificity, individual proteins were tested. Only His-MinD exhibited robust binding to the
798 liposome-coated sensor, while His-MinC and His-PDZ showed negligible signal, indicating
799 non-specific interactions (Fig. S11). These initial tests support the expected specificity of the
800 MinD:MinC and MinD:PDZ interactions.

801

802 Kinetic analysis and fitting were performed by the BLItz Pro Software (version 1.3.1.3). Data
803 was exported and visualized using GraphPad Prism version 9.4.0 for Windows, (GraphPad
804 Software).

805 The BLItz Pro Software analysis follows a 1:1 binding model, where:

$$A + B \underset{k_{\mathrm{off}}}{\overset{k_{\mathrm{on}}}{\rightleftarrows}} AB$$

806 with k_{on} = rate of association or "on-rate" and k_{off} = rate of dissociation or "off-rate".

807 Formula for fitting the association (a = slope):

$$Y = Y_0 + a\,(1 - e^{-k_{\mathrm{obs}} \times t})$$

$$k_{\mathrm{obs}} = k_{\mathrm{on}} \times [A(M)] + k_{\mathrm{off}}$$

808 Formula for fitting the dissociation:

$$Y = Y_0 + a \times e^{-k_{\mathrm{off}} \times t}$$

809 Resulting in the equilibrium dissociation constant K_{D}:

$$K_{\mathrm{D}} = \frac{k_{\mathrm{off}}}{k_{\mathrm{on}}}$$

810

811 **Fluorescence microscopy**

812 **Microscopy slide preparation**

813 For epifluorescence imaging, *B. subtilis* cells were mounted on 1.5% MD agarose pads using
814 1.5 x 1.6 cm "Gene Frames" (Thermo Scientific), and incubated 10 min at 37°C before
815 microscopic analysis.

816 For SMLM, slides and coverslips were first cleaned by overnight storage in 1 M KOH,
817 carefully rinsed with ddH2O, and subsequently dried with pressurized air. Next, 1.5% (w/v)
818 low melting agarose (Sigma-Aldrich) was dissolved in MD medium. Medium was sterile
819 filtered (0.2 µm pore size) shortly before being used to remove particles. To produce flat,
820 uniform, and reproducible agarose pads, 1.5 x 1.6 cm "Gene Frames" (Thermo Fisher) were
821 utilized, and pads were allowed to solidify for 1 h at room temperature to be used within the
822 next 3 h.

823 **Staining of HaloTag**

824 For staining, 1 mL of bacterial culture was moved to a 2 mL microcentrifuge tube and
825 incubated with 5 nM (SMLM) or 50 nM (epifluorescence) HaloTag TMR ligand at 37 °C for 10
826 min. Cells were harvested (4000 g, 3 min, 37 °C) and washed four times in pre-warmed MD
827 medium, before being mounted on the previously described microscopy slides.

828 **Epifluorescence imaging**

829 For strain characterization (Fig. 2 B), microscopy images were taken on a Axio Observer 7
830 microscope (Zeiss) equipped with a Colibri 7 LED light source (Zeiss) and an OrcaR^2 camera
831 (Hamamatsu) using a Plan-Apochromat 100×/1.4 oil Ph3 objective (Zeiss). TMR fluorescence
832 was visualized with a 90 HE LED filter set (QBP 425/30 + 514/30 + 592/30 + 709/100) (Zeiss)
833 and excited at 555 nm (100% intensity of Colibri 7 LED) for 400 ms. The microscope was
834 equipped with an environmental chamber set to 37 °C. Digital images were acquired with
835 Zen Blue (Zeiss) and analyzed and edited with Fiji (104) ImageJ2 (105). For measurement of
836 cell length and minicells, cells were stained with NileRed (1 µg/ml final concentration) at
837 OD_{600} 0.5 and incubated for further 20 minutes (200 rpm, 37°C) before mounting them on an
838 agarose pad. To minimize bias during analysis, cell lengths and number of minicells were
839 identified using the Fiji (104) plugin MicrobeJ 5.11c (106) on phase contrast images with
840 manual correction by screening the results against the simultaneously acquired membrane
841 stain images and sorting out mislabeled cells. For cell length measurements, MicrobeJ
842 modules *options*, *exclude on edges*, *shape descriptor*, *segmentation* and *chain* were used
843 with default settings, except for following parameters in *options* (*area* 1-max; *length* 1-max;
844 *width* 0.6-1; *sinuosity* 1-max; *angularity* 0-0.5) and *chain* (*tolerance* 0.1; *area* 1.5-max). To
845 identify minicells, MicrobeJ modules *options*, *exclude on edges*, *shape descriptor* and

846 *segmentation* were used with default settings, except for following parameters in *options*
847 (*area* 0.15-1; *length* 0.5-1.2; *width* 0.3-1; *circularity* 0.95-max).

848 **SMLM imaging**

849 SMLM imaging was performed with an Elyra 7 (Zeiss) inverted microscope equipped with
850 two pco.edge sCMOS 4.2 CL HS cameras (PCO AG), connected through a DuoLink (Zeiss), only
851 one of which was used in this study. Cells were observed through an alpha Plan-Apochromat
852 63x/1.46 Oil Korr M27 Var2 objective, yielding a final pixel size of 97 nm. During image
853 acquisition, the focus was maintained with the help of a Definite Focus.2 system (Zeiss).
854 Fluorescence was excited with a 561 nm (100 mW) laser, and signals were observed through
855 a multiple beam splitter (405/488/561/641 nm) and laser block filters (405/488/561/641
856 nm) followed by a Duolink SR QUAD (Zeiss) filter module (secondary beam splitter: LP 560,
857 emission filters: EF BP420-480 + BP495-550).

858 Cells were illuminated with the 561 nm laser (50% intensity) in TIRF mode (62° angle). For
859 each time lapse series 10,000 frames were taken with 20 ms exposure time (~24 ms with
860 transfer time included) and 50% 561 nm intensity laser.

861 **SMLM analysis**

862 For average localization analysis (Fig. 4 A), a single-molecule localization table was
863 constructed from a 2D Gaussian fitting in the ZEN 3.0 SR (black) software (Zeiss) with a peak
864 mask size of 9 and a peak intensity-to-noise ratio of 6, and further allowing molecules to
865 overlap. Filtering was used to minimize noise, background, and out-of-focus emitters,
866 discarding events that did not emit within a Point spread function size (PSF) of 100-200 nm
867 and did not display a photon count of 50-600. Further analysis was performed using
868 individual Fiji (104) scripts for the cell outlines and R (4.2.2) scripts in R Studio

869 (2023.12.1+402) for the corresponding localization events (107, 108). Here, the remaining
870 events were transformed to align the orientation of all cells in which the signals were
871 detected, to be able to summarize all recorded localizations in one normalized cell per strain.
872 The localization frequency is displayed as a heatmap using the gradual viridis scaling from
873 the ggplot2 R package (109), where the highest frequency (normalized frequency 1) is
874 displayed in yellow and the lowest frequency (normalized frequency 0) in blue (Fig. 4 A).

875 For single-molecule tracking, spots were identified with the LoG Detector of TrackMate
876 v6.0.1 (110) implemented in Fiji 1.53 g (104), an estimated diameter of 0.5 µm, and median
877 filter and sub-pixel localization activated. The signal-to-noise threshold for the identification
878 of the spots was set at 7. To limit the detection of particles to single-molecules, frames
879 belonging to the bleaching phase of TMR were removed individually from the time lapses
880 prior to the identification of spots. Spots were merged into tracks via the "Simple LAP
881 Tracker" of TrackMate, with a maximum linking distance of 500 nm and no frame gaps
882 allowed. Only tracks with a minimum length of 5 frames were used for further analysis,
883 yielding a minimum number of total tracks per sample of 2596.

884 To identify differences in protein mobility and/or behavior, the resulting tracks were
885 subjected to stationary localization analysis (SLA), mean-squared-displacement (MSD) and
886 square displacement (SQD) analysis in SMTracker 2.0 (74). SLA analysis was performed with
887 a confinement circle radius of 97 nm and a minimum number of 5 steps to be considered
888 static. The average MSD was calculated for four separate time points per strain (exposure of
889 20 ms - τ = 24, 48, 72 and 96 ms), followed by fitting of the data to a linear equation. The last
890 time point of each track was excluded to avoid track-ending-related artifacts. The cumulative
891 probability distribution of the square displacements (SQD) was used to estimate the
892 diffusion constants and relative fractions of up to three diffusive states. Diffusion constants

were determined simultaneously for the compared conditions, therefore allowing for a more direct population fractions comparison. Additionally, the analysis was performed for each strain non-comparatively, yielding individual diffusion coefficients, displayed in Tab. 3**Error! Reference source not found.**.

Acknowledgments

This research was supported by the Deutsche Forschungsgemeinschaft (DFG) within the Transregio Collaborative Research Center (TRR 174) “Spatiotemporal Dynamics of Bacterial Cells”. We thank Leendert Hamoen (Amsterdam) and Henrik Strahl (Newcastle) for communicating unpublished results prior to publication. We are also grateful to Anna Becker and Vivian Hennig (Kiel) for help in the initial stages of this project as part of their BSc theses.

Author Contributions

M.B. and H.F. conceived the study, H.F. constructed the strains, performed the *in vivo* and *in vitro* experiments incl. microscopy. C.D. performed *in vitro* experiments. H.F., C.D. and M.B. analyzed the data, H.F. and M.B. wrote the manuscript.

Declaration of Interests

The authors declare no competing interests.

Figure legends

Fig. 1: Biochemical analysis of *B. subtilis* MinD ATPase cycle.

(A) Phosphate release plotted against different MinD concentrations, fitted with a simple linear regression (R^2 = 0.97). Phosphate release was measured using the EnzChek™ phosphate assay kit. Samples contained 0.2 mg ml^{-1} liposomes and were pre-incubated for 10 minutes before addition of 2 mM Mg^{2+}-ATP; n ≥ 3.

(B) Specific activity of the MinD ATPase from (A) measured as a function of MinD concentration.

(C) Specific activity of MinD measured as a function of ATP concentration, determined as in (B) with fixed MinD concentration of 10 µM. Fitting the Michaelis–Menten equation (black lines) gives k_{cat} = 36.27 h^{-1}, V_{max} = 19.50 nmol mg^{-1} min^{-1} and K_M = 0.173 mM.

(D) Specific activity of MinD measured as a function of liposome concentration, determined as in (B) with fixed MinD concentration of 6 µM. Fitting the Michaelis–Menten equation (black lines) gives k_{cat} = 41.01 h^{-1}, V_{max} = 22.05 nmol mg^{-1} min^{-1} and K_M = 0.0437 mg ml^{-1}.

932 **Fig. 2: Cartoon of MinD AlphaFold model with highlighted key amino acids and the effects**
933 **of their mutagenesis.**

934 (A) Left: Rendering of MinD AlphaFold model with ATP binding region highlighted in light
935 blue, membrane targeting sequence (MTS) in turquoise and key residues in orange; Box:
936 explanation of mutagenesis effects. Right: Close-up on hydrophobic region of amphipathic
937 helix.

938 (B) Representative wide-field microscopy images of *B. subtilis* expressing indicated Halo-
939 MinD variants as the only MinD copy from the native locus, stained with TMR ligand. Left:
940 Phase contrast; scale bar 5 µm. Right: fluorescence.

941

942

943 **Fig. 3: BLI analysis of His-MinD and different mutants.**

944 (A) Left: Cartoon representation of the different BLI steps, starting with (1) establishing a
945 baseline in protein buffer, (2) binding of liposomes through the biotinylated DSPE-PEG(2000)
946 phospholipid, (3) establishing a new baseline, (4) binding of MinD and finally (5) dissociation
947 of MinD. Right: Exemplary graph resulting from sensor readouts of steps (1) - (5). Scheme
948 adapted from (102).

949 (B) MinD binding plotted against time through association and dissociation phase (steps 4-5)
950 at different protein concentrations, including the His-MinD-I260E mutant.

951 (C) – (E) Same as (B) using the indicated respective mutant of His-MinD (G12V, K16A and
952 D40A).

953 **Fig. 4: Single-molecule localization microscopy analysis of Halo-MinD and mutants**
954 **expressed in *B. subtilis*.**

955 Exponentially growing *B. subtilis* cells expressing Halo-MinD and variants (n ≥ 48 cells,
956 respectively) were stained with TMR ligand and subsequently imaged. Individual protein
957 trajectories were recorded using SMLM and analyzed with Zen blue (Zeiss), Trackmate, the
958 SMTracker 2.0 software package and manual scripts in R. Minimum track-length 4 frames of
959 24 ms, with at least 2596 trajectories per strain.

960 (A) Heat map representation of intracellular localization of individual molecules of Halo-
961 MinD and variants, respectively, plotted on normalized cells. Brighter colors indicate higher
962 abundance.

963 (B) Barplot of stationary localization analysis (SLA), comparing different track types within
964 the protein population. Tracks were considered static when not leaving a circular area of 97
965 nm diameter within 5+ frames. Mobile populations were further divided into free and mixed
966 tracks, where mixed tracks displayed a switch between free and confined movement.

967 (C) Plot of the mean-squared displacement of Halo-MinD and variants over time, fitted with
968 a linear fit excluding the last timelag.

969 (D) Bubble plot displaying single-molecule diffusion rates of the indicated MinD fusions.
970 Populations were determined by fitting the probability distributions of the frame-to-frame
971 displacement (jump distance) data of all respective tracks to a three components model (fast
972 mobile, slow mobile and confined protein populations).

973 (E) Probability distributions of jump distances of Halo-MinD and variants. Data was fit with a
974 three component model, indicating confined, slow and fast tracks.

Tables

Tab. 1: Kinetic constants of His-MinD and variants obtained via BLI.

Protein	K_D [µM]	k_{on} [M^{-1} s^{-1}]	$k_{on\ error}$	k_{off} [s^{-1}]	$k_{off\ error}$	X^2	R^2
MinD	7.17	3.03×10^3	0.13×10^3	21.7×10^{-3}	0.33×10^{-3}	16.07	0.95
MinD-G12V	75.38	0.63×10^3	0.19×10^3	47.8×10^{-3}	1.13×10^{-3}	13.89	0.95
MinD-K16A	1.36	2.03×10^3	0.062×10^3	2.77×10^{-3}	0.088×10^{-3}	6.97	0.95
MinD-D40A	0.74	2.39×10^3	0.053×10^3	1.76×10^{-3}	0.069×10^{-3}	6.01	0.98
MinD-I260E	74.36	0.18×10^3	0.19×10^3	13.45×10^{-3}	0.38×10^{-3}	3.61	0.95

K_D = equilibrium dissociation constant; k_{on} = association rate constant; k_{off} = dissociation rate constant

980 **Tab. 2: Kinetic constants of His-MinD in combination with His-MinC or His-PDZ.**

Protein	K_D [µM]	k_{on} [M^{-1} s^{-1}]	$k_{on\ error}$	k_{off} [s^{-1}]	$k_{off\ error}$	X^2	R^2
MinD*	31.7	0.27×10^3	0.21×10^3	8.65×10^{-3}	0.26×10^{-3}	4.10	0.957
+ MinC	33.4	0.35×10^3	0.084×10^3	11.7×10^{-3}	0.16×10^{-3}	8.07	0.979
MinD*	51.1	0.34×10^3	0.12×10^3	17.5×10^{-3}	0.24×10^{-3}	2.40	0.986
+ PDZ	47.5	0.35×10^3	0.14×10^3	16.6×10^{-3}	0.25×10^{-3}	8.98	0.973

981 K_D = equilibrium dissociation constant; k_{on} = association rate constant; k_{off} = dissociation rate
982 constant. *His-MinD control appears twice, from independent purifications. Since batches were not
983 directly comparable, controls are only compared to samples containing the same batch.
984 Concentrations: His-MinD 8 µM, His-MinC 1-16 µM [1, 2, 4, 8 & 16], His-PDZ 1-16 µM [1, 2, 4, 8 & 16],
985 see Fig. S 11.

986

987 **Tab. 3: Diffusion coefficients obtained from non-comparative SQD analysis of Halo-MinD**
988 **and variants fitted with three populations.**

Strain	Fast diffusive [$\mu m^2 s^{-1}$]	Slow diffusive [$\mu m^2 s^{-1}$]	Confined [$\mu m^2 s^{-1}$]
MinD WT	0.60 (22.3 %)	0.084 (50.4 %)	0.020 (27.3 %)
MinD-G12V	0.68 (28.5 %)	0.10 (47.5 %)	0.026 (24.0 %)
MinD-K16A	0.70 (27.3 %)	0.11 (43.9 %)	0.024 (28.8 %)
MinD-D40A	0.44 (13.7 %)	0.063 (50.0 %)	0.021 (36.3 %)
MinD-I260E	0.76 (73.4 %)	0.095 (20.3 %)	0.022 (6.3 %)

989 Percentages indicate relative population size

990 **Tab. 4: Diffusion coefficients obtained from non-comparative SQD analysis of Halo-MinD in**
991 **different genetic backgrounds fitted with three populations.**

Strain	Fast diffusive [$\mu m^2 s^{-1}$]	Slow diffusive [$\mu m^2 s^{-1}$]	Confined [$\mu m^2 s^{-1}$]
WT	0.57 (22.1 %)	0.083 (50.2 %)	0.019 (27.7 %)
Δ*minC*	0.31 (29.3 %)	0.059 (44.3 %)	0.01 (26.4 %)
Δ*minJ*	0.6 (19 %)	0.069 (41.2 %)	0.018 (39.7 %)

992 Percentages indicate relative population size

References

1. Kotak S, Gonczy P. 2013. Mechanisms of spindle positioning: cortical force generators in the limelight. Curr Opin Cell Biol 25:741-8.
2. Pollard TD, O'Shaughnessy B. 2019. Molecular Mechanism of Cytokinesis. Annu Rev Biochem 88:661-689.
3. Cameron TA, Margolin W. 2024. Insights into the assembly and regulation of the bacterial divisome. Nat Rev Microbiol 22:33-45.
4. Mahone CR, Goley ED. 2020. Bacterial cell division at a glance. J Cell Sci 133.
5. den Blaauwen T, Hamoen LW, Levin PA. 2017. The divisome at 25: the road ahead. Curr Opin Microbiol 36:85-94.
6. Bi EF, Lutkenhaus J. 1991. FtsZ ring structure associated with division in Escherichia coli. Nature 354:161-4.
7. Lowe J, Amos LA. 1998. Crystal structure of the bacterial cell-division protein FtsZ. Nature 391:203-6.
8. Schaper S, Brito AD, Saraiva BM, Squyres GR, Holmes MJ, Garner EC, Hensel Z, Henriques R, Pinho MG. 2024. Cell constriction requires processive septal peptidoglycan synthase movement independent of FtsZ treadmilling in Staphylococcus aureus. Nat Microbiol 9:1049-1063.
9. Whitley KD, Jukes C, Tregidgo N, Karinou E, Almada P, Cesbron Y, Henriques R, Dekker C, Holden S. 2021. FtsZ treadmilling is essential for Z-ring condensation and septal constriction initiation in Bacillus subtilis cell division. Nat Commun 12:2448.
10. Squyres GR, Holmes MJ, Barger SR, Pennycook BR, Ryan J, Yan VT, Garner EC. 2021. Single-molecule imaging reveals that Z-ring condensation is essential for cell division in Bacillus subtilis. Nat Microbiol 6:553-562.
11. Egan AJF, Errington J, Vollmer W. 2020. Regulation of peptidoglycan synthesis and remodelling. Nat Rev Microbiol 18:446-460.
12. Adams DW, Errington J. 2009. Bacterial cell division: assembly, maintenance and disassembly of the Z ring. Nat Rev Microbiol 7:642-53.
13. Chan H, Mohamed AMT, Grainge I, Rodrigues CDA. 2022. FtsK and SpoIIIE, coordinators of chromosome segregation and envelope remodeling in bacteria. Trends Microbiol 30:480-494.
14. Reyes-Lamothe R, Sherratt DJ. 2019. The bacterial cell cycle, chromosome inheritance and cell growth. Nat Rev Microbiol 17:467-478.
15. Bramkamp M, van Baarle S. 2009. Division site selection in rod-shaped bacteria. Curr Opin Microbiol 12:683-8.
16. Szwedziak P, Ghosal D. 2017. FtsZ-ring Architecture and Its Control by MinCD. Subcell Biochem 84:213-244.
17. Ortiz C, Natale P, Cueto L, Vicente M. 2016. The keepers of the ring: regulators of FtsZ assembly. FEMS Microbiol Rev 40:57-67.
18. Rodrigues CD, Harry EJ. 2012. The Min system and nucleoid occlusion are not required for identifying the division site in *Bacillus subtilis* but ensure its efficient utilization. PLoS Genet 8:e1002561.
19. Wu LJ, Errington J. 2011. Nucleoid occlusion and bacterial cell division. Nat Rev Microbiol 10:8-12.
20. Bernhardt TG, de Boer PA. 2005. SlmA, a nucleoid-associated, FtsZ binding protein required for blocking septal ring assembly over Chromosomes in E. coli. Mol Cell 18:555-64.
21. Cho H, McManus HR, Dove SL, Bernhardt TG. 2011. Nucleoid occlusion factor SlmA is a DNA-activated FtsZ polymerization antagonist. Proc Natl Acad Sci U S A 108:3773-8.

1042 22. Tonthat NK, Arold ST, Pickering BF, Van Dyke MW, Liang S, Lu Y, Beuria TK, Margolin W,
1043 Schumacher MA. 2011. Molecular mechanism by which the nucleoid occlusion factor, SlmA,
1044 keeps cytokinesis in check. EMBO J 30:154-64.
1045 23. Wu LJ, Errington J. 2004. Coordination of cell division and chromosome segregation by a
1046 nucleoid occlusion protein in Bacillus subtilis. Cell 117:915-25.
1047 24. Wu LJ, Ishikawa S, Kawai Y, Oshima T, Ogasawara N, Errington J. 2009. Noc protein binds to
1048 specific DNA sequences to coordinate cell division with chromosome segregation. EMBO J
1049 28:1940-52.
1050 25. Jalal ASB, Tran NT, Wu LJ, Ramakrishnan K, Rejzek M, Gobbato G, Stevenson CEM, Lawson
1051 DM, Errington J, Le TBK. 2021. CTP regulates membrane-binding activity of the nucleoid
1052 occlusion protein Noc. Mol Cell 81:3623-3636 e6.
1053 26. Adams DW, Wu LJ, Errington J. 2015. Nucleoid occlusion protein Noc recruits DNA to the
1054 bacterial cell membrane. EMBO J 34:491-501.
1055 27. Adler HI, Fisher WD, Cohen A, Hardigree AA. 1967. MINIATURE escherichia coli CELLS
1056 DEFICIENT IN DNA. Proc Natl Acad Sci U S A 57:321-6.
1057 28. Schaumberg TH, Kuempel PL. 1983. Genetic mapping of the minB locus in Escherichia coli K-
1058 12. J Bacteriol 153:1063-5.
1059 29. Davie E, Sydnor K, Rothfield LI. 1984. Genetic basis of minicell formation in Escherichia coli K-
1060 12. J Bacteriol 158:1202-3.
1061 30. de Boer PA, Crossley RE, Rothfield LI. 1989. A division inhibitor and a topological specificity
1062 factor coded for by the minicell locus determine proper placement of the division septum in
1063 E. coli. Cell 56:641-9.
1064 31. de Boer PA, Crossley RE, Rothfield LI. 1992. Roles of MinC and MinD in the site-specific
1065 septation block mediated by the MinCDE system of Escherichia coli. J Bacteriol 174:63-70.
1066 32. Hu Z, Mukherjee A, Pichoff S, Lutkenhaus J. 1999. The MinC component of the division site
1067 selection system in Escherichia coli interacts with FtsZ to prevent polymerization. Proc Natl
1068 Acad Sci U S A 96:14819-24.
1069 33. Cordell SC, Anderson RE, Lowe J. 2001. Crystal structure of the bacterial cell division inhibitor
1070 MinC. EMBO J 20:2454-61.
1071 34. Hu Z, Lutkenhaus J. 2000. Analysis of MinC reveals two independent domains involved in
1072 interaction with MinD and FtsZ. J Bacteriol 182:3965-71.
1073 35. Shen B, Lutkenhaus J. 2009. The conserved C-terminal tail of FtsZ is required for the septal
1074 localization and division inhibitory activity of MinC(C)/MinD. Mol Microbiol 72:410-24.
1075 36. Shen B, Lutkenhaus J. 2010. Examination of the interaction between FtsZ and MinCN in E. coli
1076 suggests how MinC disrupts Z rings. Mol Microbiol 75:1285-98.
1077 37. Marston AL, Errington J. 1999. Selection of the midcell division site in Bacillus subtilis through
1078 MinD-dependent polar localization and activation of MinC. Mol Microbiol 33:84-96.
1079 38. Gregory JA, Becker EC, Pogliano K. 2008. Bacillus subtilis MinC destabilizes FtsZ-rings at new
1080 cell poles and contributes to the timing of cell division. Genes Dev 22:3475-88.
1081 39. Scheffers DJ. 2008. The effect of MinC on FtsZ polymerization is pH dependent and can be
1082 counteracted by ZapA. FEBS Lett 582:2601-8.
1083 40. de Boer PA, Crossley RE, Hand AR, Rothfield LI. 1991. The MinD protein is a membrane
1084 ATPase required for the correct placement of the Escherichia coli division site. EMBO J
1085 10:4371-80.
1086 41. Marston AL, Thomaides HB, Edwards DH, Sharpe ME, Errington J. 1998. Polar localization of
1087 the MinD protein of Bacillus subtilis and its role in selection of the mid-cell division site.
1088 Genes Dev 12:3419-30.
1089 42. Pulianmackal LT, Vecchiarelli AG. 2024. Positioning of cellular components by the ParA/MinD
1090 family of ATPases. Curr Opin Microbiol 79:102485.
1091 43. Lutkenhaus J. 2012. The ParA/MinD family puts things in their place. Trends Microbiol
1092 20:411-8.

1093 44. Szardenings F, Guymer D, Gerdes K. 2011. ParA ATPases can move and position DNA and
1094 subcellular structures. Curr Opin Microbiol 14:712-8.
1095 45. Szeto TH, Rowland SL, Habrukowich CL, King GF. 2003. The MinD membrane targeting
1096 sequence is a transplantable lipid-binding helix. J Biol Chem 278:40050-6.
1097 46. Szeto TH, Rowland SL, Rothfield LI, King GF. 2002. Membrane localization of MinD is
1098 mediated by a C-terminal motif that is conserved across eubacteria, archaea, and
1099 chloroplasts. Proc Natl Acad Sci U S A 99:15693-8.
1100 47. Zhou H, Lutkenhaus J. 2004. The switch I and II regions of MinD are required for binding and
1101 activating MinC. J Bacteriol 186:1546-55.
1102 48. Raskin DM, de Boer PA. 1999. Rapid pole-to-pole oscillation of a protein required for
1103 directing division to the middle of Escherichia coli. Proc Natl Acad Sci U S A 96:4971-6.
1104 49. Hale CA, Meinhardt H, de Boer PA. 2001. Dynamic localization cycle of the cell division
1105 regulator MinE in Escherichia coli. EMBO J 20:1563-72.
1106 50. Hu Z, Lutkenhaus J. 1999. Topological regulation of cell division in Escherichia coli involves
1107 rapid pole to pole oscillation of the division inhibitor MinC under the control of MinD and
1108 MinE. Mol Microbiol 34:82-90.
1109 51. Loose M, Fischer-Friedrich E, Ries J, Kruse K, Schwille P. 2008. Spatial regulators for bacterial
1110 cell division self-organize into surface waves in vitro. Science 320:789-92.
1111 52. Varley AW, Stewart GC. 1992. The divIVB region of the Bacillus subtilis chromosome encodes
1112 homologs of Escherichia coli septum placement (minCD) and cell shape (mreBCD)
1113 determinants. J Bacteriol 174:6729-42.
1114 53. Levin PA, Margolis PS, Setlow P, Losick R, Sun D. 1992. Identification of Bacillus subtilis genes
1115 for septum placement and shape determination. J Bacteriol 174:6717-28.
1116 54. Lee S, Price CW. 1993. The minCD locus of Bacillus subtilis lacks the minE determinant that
1117 provides topological specificity to cell division. Mol Microbiol 7:601-10.
1118 55. Patrick JE, Kearns DB. 2008. MinJ (YvjD) is a topological determinant of cell division in Bacillus
1119 subtilis. Mol Microbiol 70:1166-79.
1120 56. Bramkamp M, Emmins R, Weston L, Donovan C, Daniel RA, Errington J. 2008. A novel
1121 component of the division-site selection system of Bacillus subtilis and a new mode of action
1122 for the division inhibitor MinCD. Mol Microbiol 70:1556-69.
1123 57. van Baarle S, Bramkamp M. 2010. The MinCDJ system in Bacillus subtilis prevents minicell
1124 formation by promoting divisome disassembly. PLoS One 5:e9850.
1125 58. Yu Y, Zhou J, Dempwolff F, Baker JD, Kearns DB, Jacobson SC. 2020. The Min System
1126 Disassembles FtsZ Foci and Inhibits Polar Peptidoglycan Remodeling in Bacillus subtilis. mBio
1127 11.
1128 59. Bach JN, Albrecht N, Bramkamp M. 2014. Imaging DivIVA dynamics using photo-convertible
1129 and activatable fluorophores in Bacillus subtilis. Front Microbiol 5:59.
1130 60. Giacomelli G, Feddersen H, Peng F, Martins GB, Grafemeyer M, Meyer F, Mayer B, Graumann
1131 PL, Bramkamp M. 2022. Subcellular Dynamics of a Conserved Bacterial Polar Scaffold Protein.
1132 Genes (Basel) 13.
1133 61. Feddersen H, Wurthner L, Frey E, Bramkamp M. 2021. Dynamics of the Bacillus subtilis Min
1134 System. mBio 12.
1135 62. Ishikawa K, Matsuoka S, Hara H, Matsumoto K. 2017. Septal membrane localization by C-
1136 terminal amphipathic alpha-helices of MinD in Bacillus subtilis mutant cells lacking MinJ or
1137 DivIVA. Genes Genet Syst 92:81-98.
1138 63. Ramm B, Glock P, Schwille P. 2018. In Vitro Reconstitution of Self-Organizing Protein Patterns
1139 on Supported Lipid Bilayers. J Vis Exp doi:10.3791/58139.
1140 64. Hu Z, Lutkenhaus J. 2001. Topological regulation of cell division in *E. coli*: Spatiotemporal
1141 oscillation of MinD requires stimulation of its ATPase by MinE and phospholipid. Mol Cell
1142 7:1337-43.
1143 65. Hu Z, Lutkenhaus J. 2003. A conserved sequence at the C-terminus of MinD is required for
1144 binding to the membrane and targeting MinC to the septum. Mol Microbiol 47:345-55.

1145 66. Heermann T, Ramm B, Glaser S, Schwille P. 2020. Local Self-Enhancement of MinD
1146 Membrane Binding in Min Protein Pattern Formation. J Mol Biol 432:3191-3204.
1147 67. Ponting CP, Phillips C, Davies KE, Blake DJ. 1997. PDZ domains: targeting signalling molecules
1148 to sub-membranous sites. Bioessays 19:469-79.
1149 68. Strahl H, Hamoen LW. 2010. Membrane potential is important for bacterial cell division. Proc
1150 Natl Acad Sci U S A 107:12281-6.
1151 69. Karoui ME, Errington J. 2001. Isolation and characterization of topological specificity mutants
1152 of minD in Bacillus subtilis. Mol Microbiol 42:1211-21.
1153 70. Leonard TA, Butler PJ, Lowe J. 2005. Bacterial chromosome segregation: structure and DNA
1154 binding of the Soj dimer--a conserved biological switch. EMBO J 24:270-82.
1155 71. Wu W, Park KT, Holyoak T, Lutkenhaus J. 2011. Determination of the structure of the MinD-
1156 ATP complex reveals the orientation of MinD on the membrane and the relative location of
1157 the binding sites for MinE and MinC. Mol Microbiol 79:1515-28.
1158 72. Lackner LL, Raskin DM, de Boer PA. 2003. ATP-dependent interactions between Escherichia
1159 coli Min proteins and the phospholipid membrane in vitro. J Bacteriol 185:735-49.
1160 73. Heermann T, Steiert F, Ramm B, Hundt N, Schwille P. 2021. Mass-sensitive particle tracking
1161 to elucidate the membrane-associated MinDE reaction cycle. Nat Methods 18:1239-1246.
1162 74. Oviedo-Bocanegra LM, Hinrichs R, Rotter DAO, Dersch S, Graumann PL. 2021. Single
1163 molecule/particle tracking analysis program SMTracker 2.0 reveals different dynamics of
1164 proteins within the RNA degradosome complex in Bacillus subtilis. Nucleic Acids Res 49:e112.
1165 75. Barak LS, Webb WW. 1982. Diffusion of low density lipoprotein-receptor complex on human
1166 fibroblasts. J Cell Biol 95:846-52.
1167 76. Goulian M, Simon SM. 2000. Tracking single proteins within cells. Biophys J 79:2188-98.
1168 77. Weimann L, Ganzinger KA, McColl J, Irvine KL, Davis SJ, Gay NJ, Bryant CE, Klenerman D.
1169 2013. A quantitative comparison of single-dye tracking analysis tools using Monte Carlo
1170 simulations. PLoS One 8:e64287.
1171 78. Landge AN, Jordan BM, Diego X, Muller P. 2020. Pattern formation mechanisms of self-
1172 organizing reaction-diffusion systems. Dev Biol 460:2-11.
1173 79. St Johnston D, Nusslein-Volhard C. 1992. The origin of pattern and polarity in the Drosophila
1174 embryo. Cell 68:201-19.
1175 80. Negrete J, Jr., Oates AC. 2021. Towards a physical understanding of developmental
1176 patterning. Nat Rev Genet 22:518-531.
1177 81. Turing AM. 1990. The chemical basis of morphogenesis. 1953. Bull Math Biol 52:153-97;
1178 discussion 119-52.
1179 82. Meinhardt H, Gierer A. 2000. Pattern formation by local self-activation and lateral inhibition.
1180 Bioessays 22:753-60.
1181 83. Rowlett VW, Margolin W. 2013. The bacterial Min system. Curr Biol 23:R553-6.
1182 84. Ramm B, Heermann T, Schwille P. 2019. The E. coli MinCDE system in the regulation of
1183 protein patterns and gradients. Cell Mol Life Sci 76:4245-4273.
1184 85. Kretschmer S, Schwille P. 2016. Pattern formation on membranes and its role in bacterial cell
1185 division. Curr Opin Cell Biol 38:52-9.
1186 86. Halatek J, Brauns F, Frey E. 2018. Self-organization principles of intracellular pattern
1187 formation. Philos Trans R Soc Lond B Biol Sci 373.
1188 87. Scholefield G, Whiting R, Errington J, Murray H. 2011. Spo0J regulates the oligomeric state of
1189 Soj to trigger its switch from an activator to an inhibitor of DNA replication initiation. Mol
1190 Microbiol 79:1089-100.
1191 88. Easter J, Jr., Gober JW. 2002. ParB-stimulated nucleotide exchange regulates a switch in
1192 functionally distinct ParA activities. Mol Cell 10:427-34.
1193 89. Lim HC, Surovtsev IV, Beltran BG, Huang F, Bewersdorf J, Jacobs-Wagner C. 2014. Evidence
1194 for a DNA-relay mechanism in ParABS-mediated chromosome segregation. Elife 3:e02758.

1195 90. Loose M, Fischer-Friedrich E, Herold C, Kruse K, Schwille P. 2011. Min protein patterns
1196 emerge from rapid rebinding and membrane interaction of MinE. Nat Struct Mol Biol 18:577-
1197 83.
1198 91. Vecchiarelli AG, Li M, Mizuuchi M, Hwang LC, Seol Y, Neuman KC, Mizuuchi K. 2016.
1199 Membrane-bound MinDE complex acts as a toggle switch that drives Min oscillation coupled
1200 to cytoplasmic depletion of MinD. Proc Natl Acad Sci U S A 113:E1479-88.
1201 92. Turkowyd B, Virant D, Endesfelder U. 2016. From single molecules to life: microscopy at the
1202 nanoscale. Anal Bioanal Chem 408:6885-911.
1203 93. Yao Z, Carballido-Lopez R. 2014. Fluorescence imaging for bacterial cell biology: from
1204 localization to dynamics, from ensembles to single molecules. Annu Rev Microbiol 68:459-76.
1205 94. Bohorquez L, Strahl H, Marenduzzo D, Thiele M, Bürmann F, Hamoen L. 2024. Cyclical MinD
1206 membrane affinity differences are not necessary for MinD gradient formation in *Bacillus*
1207 *subtilis*. doi:10.1101/2024.06.11.598461. bioRxiv.
1208 95. Miyagi A, Ramm B, Schwille P, Scheuring S. 2018. High-Speed Atomic Force Microscopy
1209 Reveals the Inner Workings of the MinDE Protein Oscillator. Nano Lett 18:288-296.
1210 96. Halatek J, Frey E. 2012. Highly canalized MinD transfer and MinE sequestration explain the
1211 origin of robust MinCDE-protein dynamics. Cell Rep 1:741-52.
1212 97. Ghosal D, Trambaiolo D, Amos LA, Lowe J. 2014. MinCD cell division proteins form alternating
1213 copolymeric cytomotive filaments. Nat Commun 5:5341.
1214 98. Anagnostopoulos C, Spizizen J. 1961. Requirements for Transformation in *Bacillus subtilis*. J
1215 Bacteriol 81:741-6.
1216 99. Jumper J, Evans R, Pritzel A, Green T, Figurnov M, Ronneberger O, Tunyasuvunakool K, Bates
1217 R, Zidek A, Potapenko A, Bridgland A, Meyer C, Kohl SAA, Ballard AJ, Cowie A, Romera-
1218 Paredes B, Nikolov S, Jain R, Adler J, Back T, Petersen S, Reiman D, Clancy E, Zielinski M,
1219 Steinegger M, Pacholska M, Berghammer T, Bodenstein S, Silver D, Vinyals O, Senior AW,
1220 Kavukcuoglu K, Kohli P, Hassabis D. 2021. Highly accurate protein structure prediction with
1221 AlphaFold. Nature 596:583-589.
1222 100. Abramson J, Adler J, Dunger J, Evans R, Green T, Pritzel A, Ronneberger O, Willmore L, Ballard
1223 AJ, Bambrick J, Bodenstein SW, Evans DA, Hung CC, O'Neill M, Reiman D, Tunyasuvunakool K,
1224 Wu Z, Zemgulyte A, Arvaniti E, Beattie C, Bertolli O, Bridgland A, Cherepanov A, Congreve M,
1225 Cowen-Rivers AI, Cowie A, Figurnov M, Fuchs FB, Gladman H, Jain R, Khan YA, Low CMR,
1226 Perlin K, Potapenko A, Savy P, Singh S, Stecula A, Thillaisundaram A, Tong C, Yakneen S,
1227 Zhong ED, Zielinski M, Zidek A, Bapst V, Kohli P, Jaderberg M, Hassabis D, Jumper JM. 2024.
1228 Accurate structure prediction of biomolecular interactions with AlphaFold 3. Nature 630:493-
1229 500.
1230 101. Weiss M, Giacomelli G, Assaya MB, Grundt F, Haouz A, Peng F, Petrella S, Wehenkel AM,
1231 Bramkamp M. 2023. The MksG nuclease is the executing part of the bacterial plasmid
1232 defense system MksBEFG. Nucleic Acids Res 51:3288-3306.
1233 102. Maximova K, Reuter N, Trylska J. 2019. Peptidomimetic inhibitors targeting the membrane-
1234 binding site of the neutrophil proteinase 3. Biochim Biophys Acta Biomembr 1861:1502-
1235 1509.
1236 103. Wallner J, Lhota G, Schosserer M, Vorauer-Uhl K. 2017. An approach for liposome
1237 immobilization using sterically stabilized micelles (SSMs) as a precursor for bio-layer
1238 interferometry-based interaction studies. Colloids Surf B Biointerfaces 154:186-194.
1239 104. Schindelin J, Arganda-Carreras I, Frise E, Kaynig V, Longair M, Pietzsch T, Preibisch S, Rueden
1240 C, Saalfeld S, Schmid B, Tinevez J-Y, White DJ, Hartenstein V, Eliceiri K, Tomancak P, Cardona
1241 A. 2012. Fiji: an open-source platform for biological-image analysis. Nature Methods 9:676-
1242 682.
1243 105. Rueden CT, Schindelin J, Hiner MC, DeZonia BE, Walter AE, Arena ET, Eliceiri KW. 2017.
1244 ImageJ2: ImageJ for the next generation of scientific image data. BMC Bioinformatics 18:529.
1245 106. Ducret A, Quardokus EM, Brun YV. 2016. MicrobeJ, a tool for high throughput bacterial cell
1246 detection and quantitative analysis. Nat Microbiol 1:16077.

107. R Core Team. 2022. R: A Language and Environment for Statistical Computing. R Foundation for Statistical Computing:Vienna, Austria. https://www.R-project.org/.
108. Posit team. 2024. RStudio: Integrated Development Environment for R. Posit Software, PBC; Boston, MA; http://wwwpositco/.
109. Wickham H. 2016. ggplot2: Elegant Graphics for Data Analysis. Springer-Verlag New York:ISBN 978-3-319-24277-4, https://ggplot2.tidyverse.org.
110. Tinevez JY, Perry N, Schindelin J, Hoopes GM, Reynolds GD, Laplantine E, Bednarek SY, Shorte SL, Eliceiri KW. 2017. TrackMate: An open and extensible platform for single-particle tracking. Methods 115:80-90.

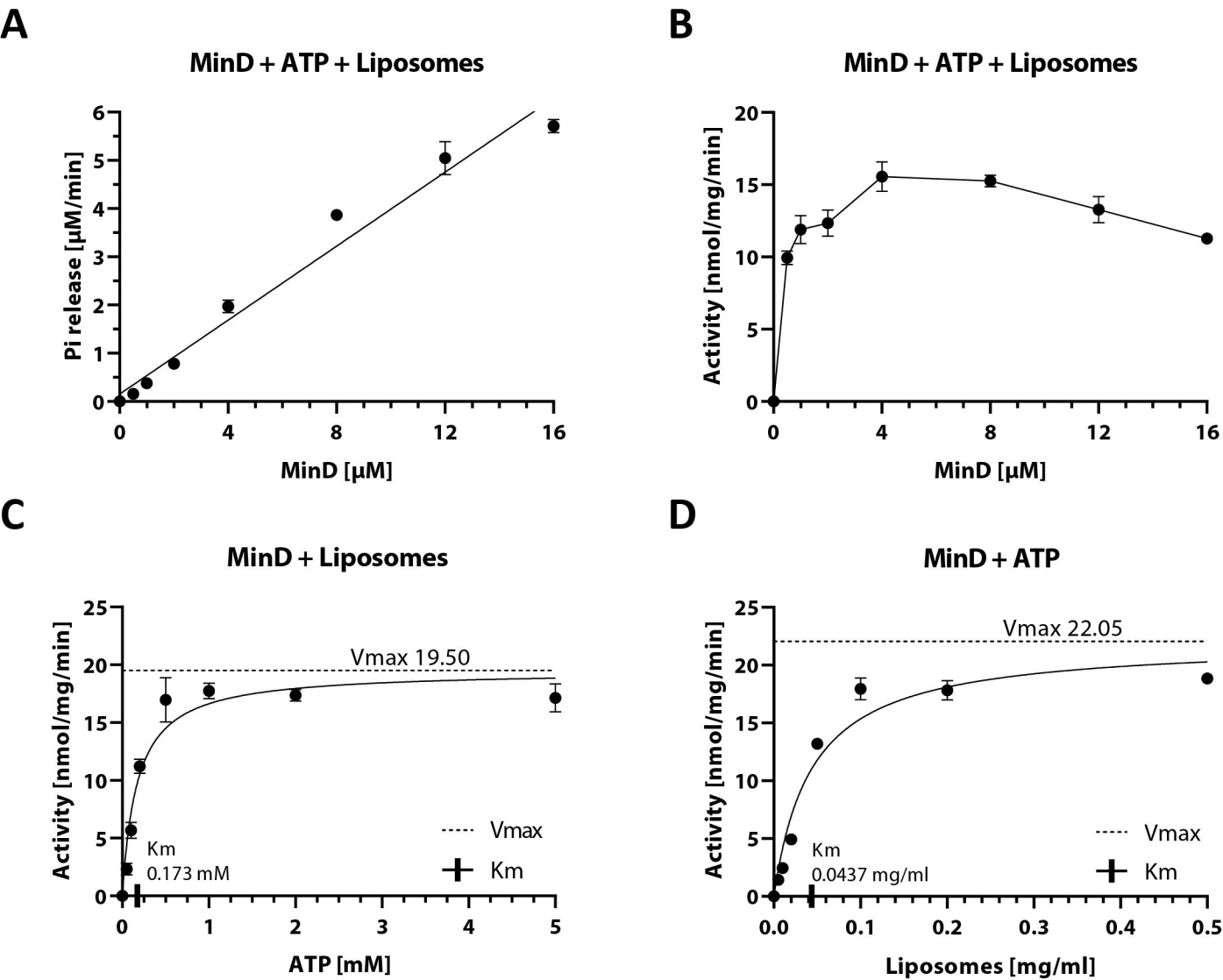
A
MinD + ATP + Liposomes
Pi release [µM/min]
MinD [µM]
B
MinD + ATP + Liposomes
Activity [nmol/mg/min]
MinD [µM]
C
MinD + Liposomes
Vmax 19.50
Km
0.173 mM
Vmax
Km
Activity [nmol/mg/min]
ATP [mM]
D
MinD + ATP
Vmax 22.05
Km
0.0437 mg/ml
Vmax
Km
Activity [nmol/mg/min]
Liposomes [mg/ml]

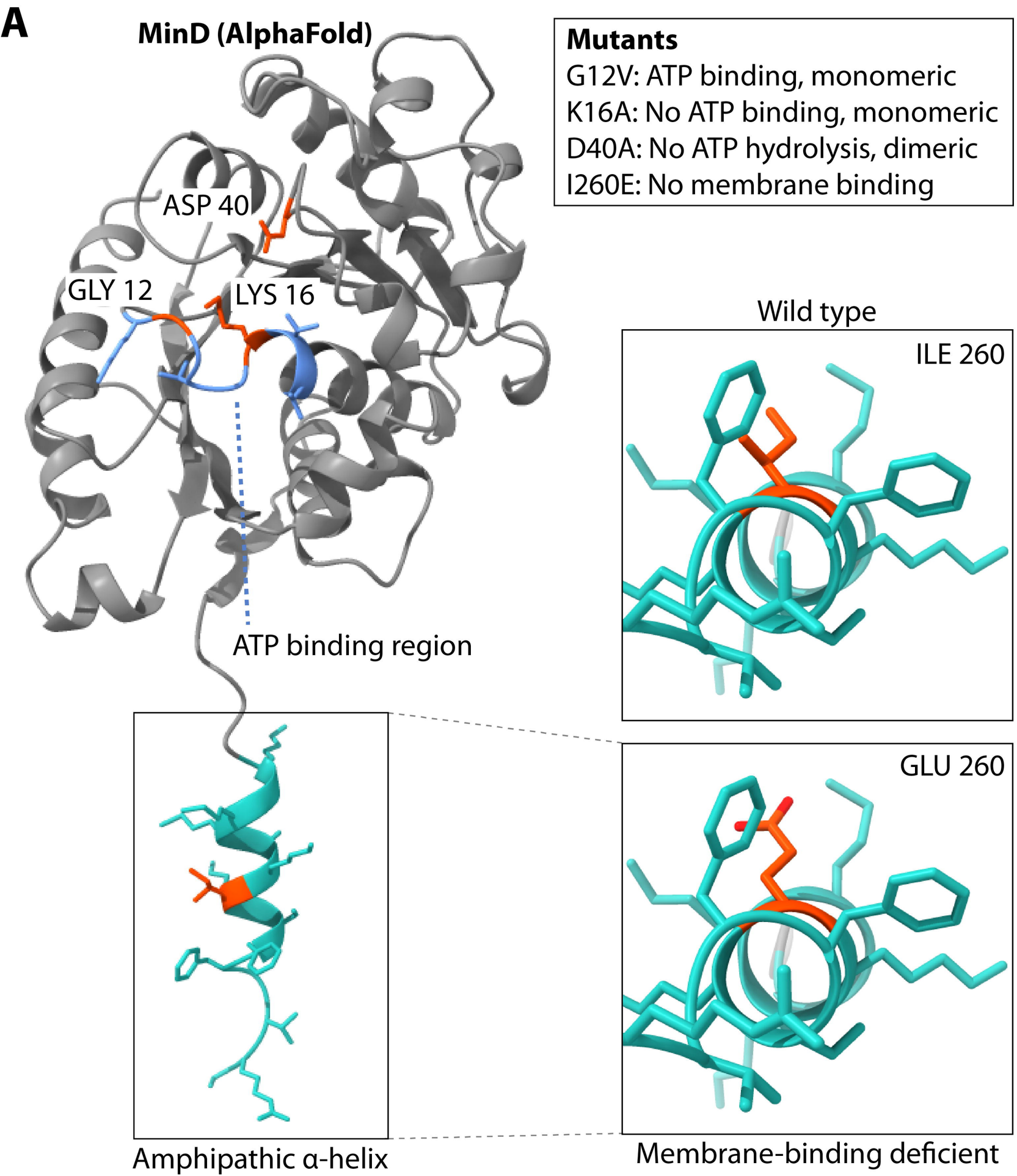
A
MinD (AlphaFold)
ASP 40
GLY 12
LYS 16
ATP binding region
Mutants
G12V: ATP binding, monomeric
K16A: No ATP binding, monomeric
D40A: No ATP hydrolysis, dimeric
I260E: No membrane binding
Wild type
ILE 260
GLU 260
Amphipathic α-helix
Membrane-binding deficient

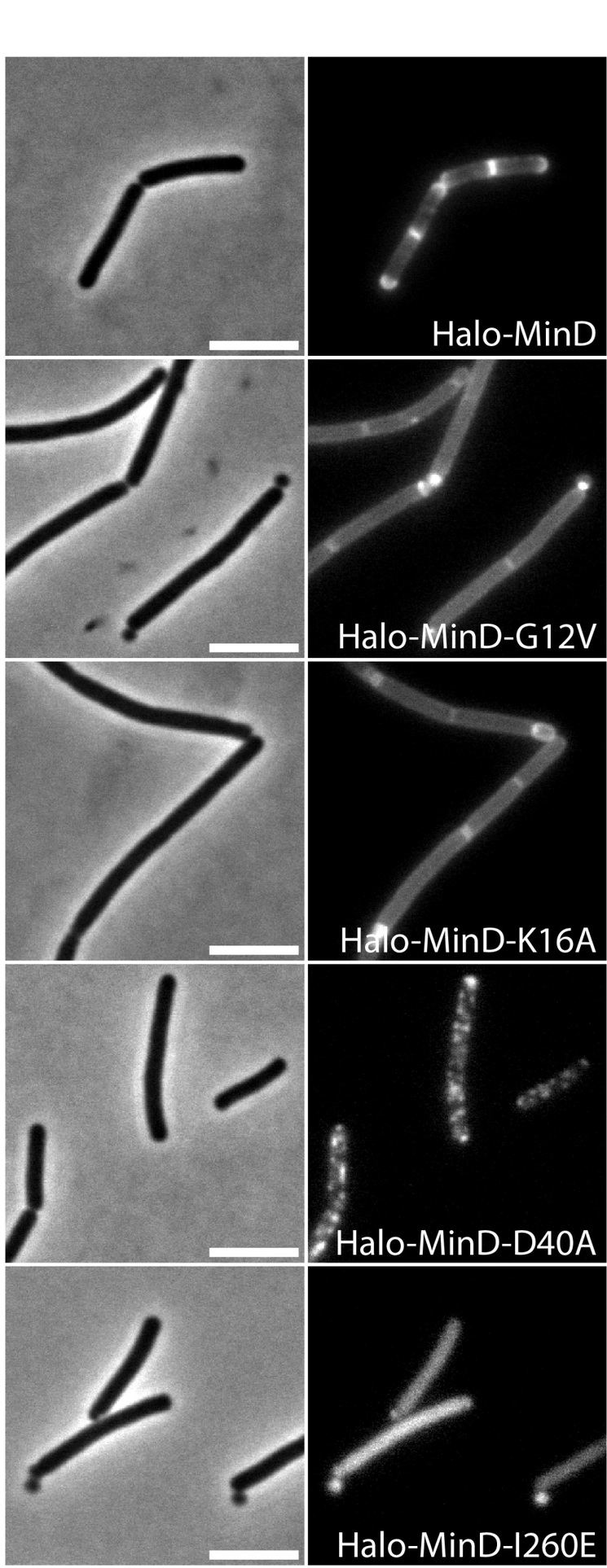
B
Halo-MinD
Halo-MinD-G12V
Halo-MinD-K16A
Halo-MinD-D40A
Halo-MinD-I260E

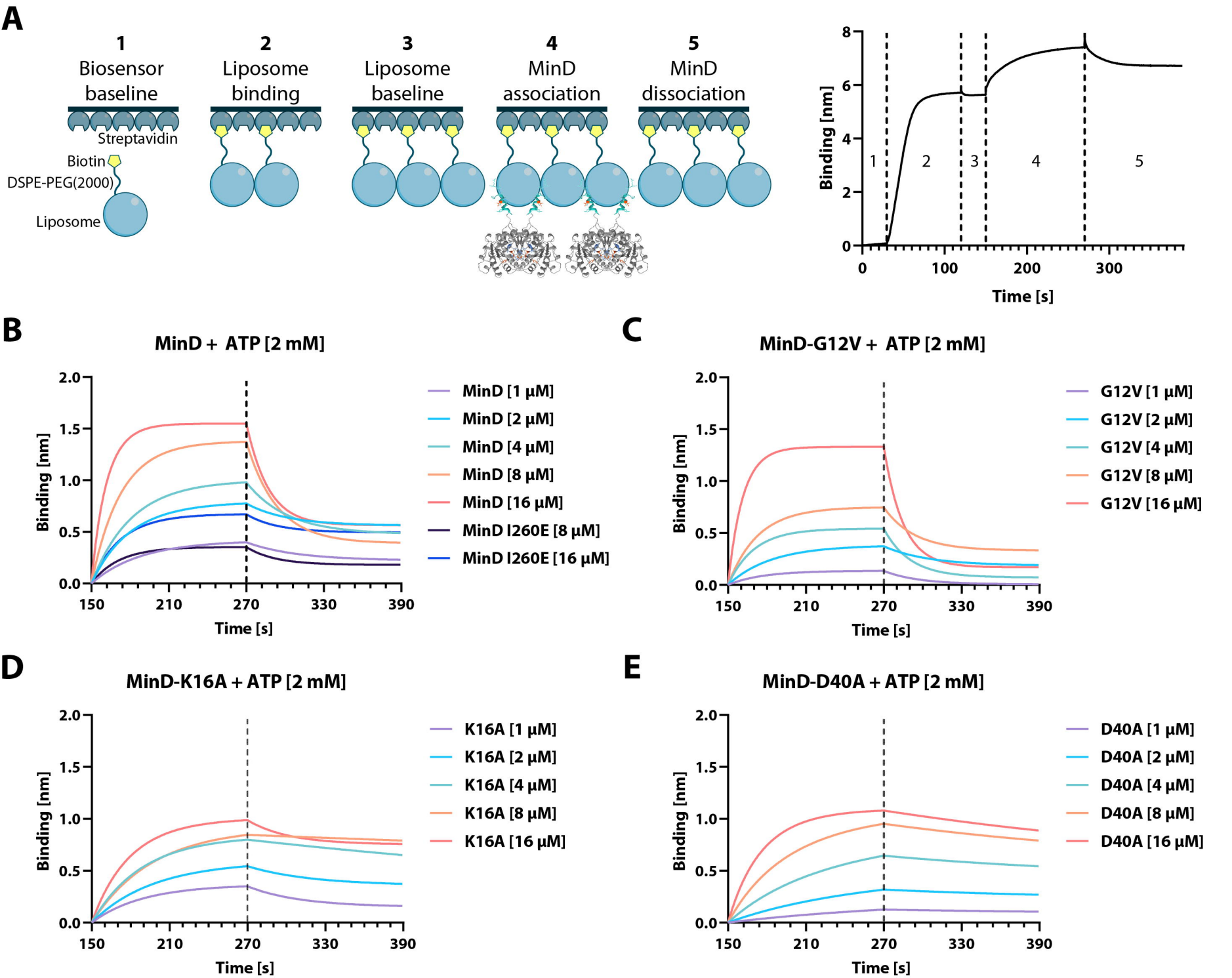
A
1
Biosensor baseline
2
Liposome binding
3
Liposome baseline
4
MinD association
5
MinD dissociation
Streptavidin
Biotin
DSPE-PEG(2000)
Liposome
Binding [nm]
Time [s]
B
MinD + ATP [2 mM]
MinD [1 µM]
MinD [2 µM]
MinD [4 µM]
MinD [8 µM]
MinD [16 µM]
MinD I260E [8 µM]
MinD I260E [16 µM]
C
MinD-G12V + ATP [2 mM]
G12V [1 µM]
G12V [2 µM]
G12V [4 µM]
G12V [8 µM]
G12V [16 µM]
D
MinD-K16A + ATP [2 mM]
K16A [1 µM]
K16A [2 µM]
K16A [4 µM]
K16A [8 µM]
K16A [16 µM]
E
MinD-D40A + ATP [2 mM]
D40A [1 µM]
D40A [2 µM]
D40A [4 µM]
D40A [8 µM]
D40A [16 µM]

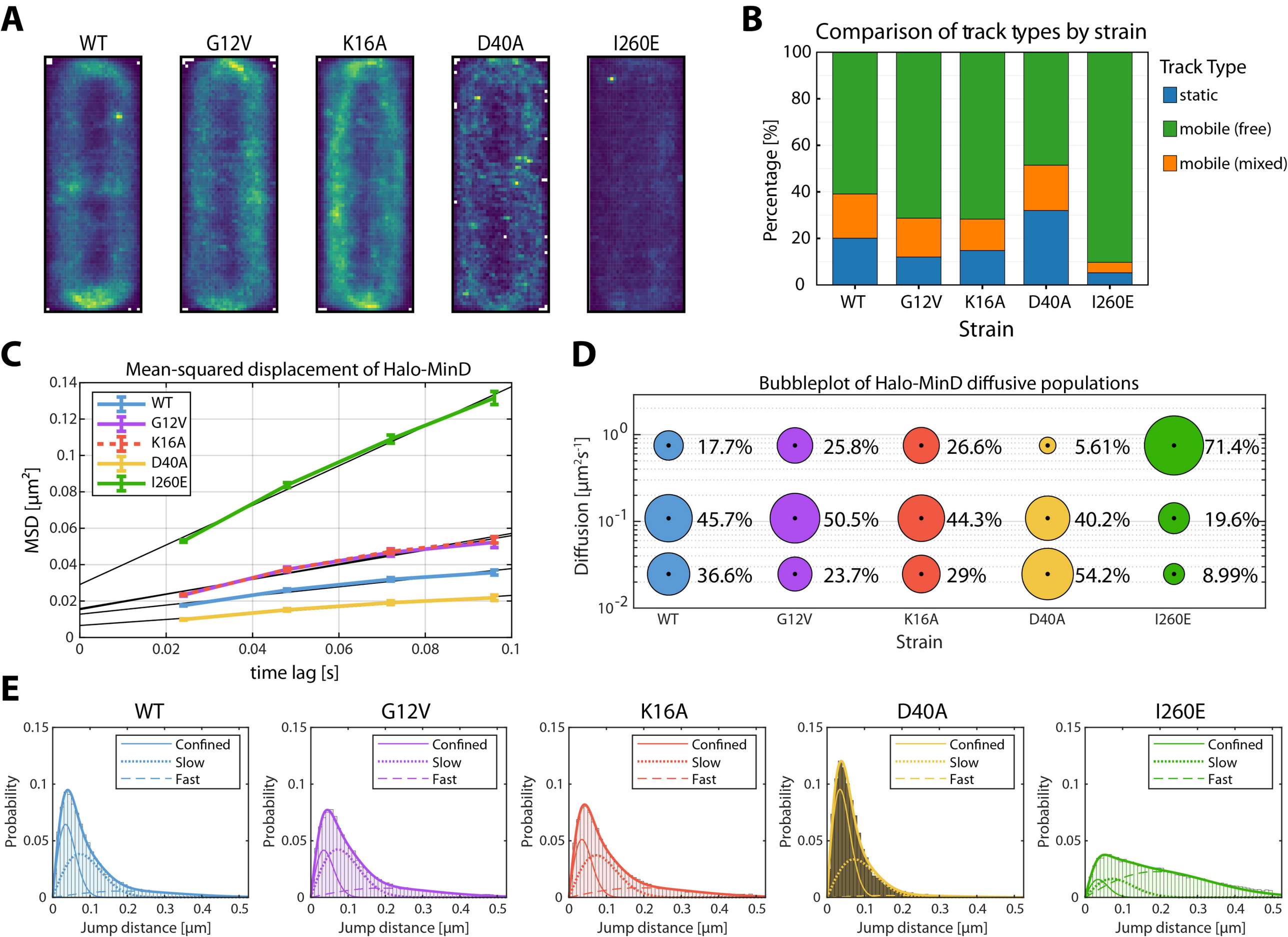
A
WT
G12V
K16A
D40A
I260E
B
Comparison of track types by strain
Percentage [%]
Strain
Track Type
static
mobile (free)
mobile (mixed)
C
Mean-squared displacement of Halo-MinD
MSD [μm²]
time lag [s]
WT
G12V
K16A
D40A
I260E
D
Bubbleplot of Halo-MinD diffusive populations
Diffusion [μm²s⁻¹]
Strain
17.7%
25.8%
26.6%
5.61%
71.4%
45.7%
50.5%
44.3%
40.2%
19.6%
36.6%
23.7%
29%
54.2%
8.99%
E
Probability
Jump distance [μm]
Confined
Slow
Fast